Applied Ocean Research 127 (2022) 103316

Contents lists available at ScienceDirect

Applied Ocean Research

journal homepage: www.elsevier.com/locate/apor

Skill assessment of different quadruplet wave-wave interaction formulations in the WAVEWATCH-III model with application to the Gulf of Mexico

Mostafa Beyramzadeh, Seyed Mostafa Siadatmousavi *

School of Civil Engineering, Iran University of Science & Technology, Narmak, Tehran, Iran, 1684613114

ARTICLE INFO

Keywords:
Gulf of Mexico
WAVEWATCH-III
ST3
ST6
Hurricane Harvey
Hurricane Irma
ERA5
GQM

ABSTRACT

In this study, the Gaussian Quadrature Method (GQM) method was implemented in the WAVEWATCH-III model and used along with embedded formulations for estimating the nonlinear wave interactions. The results of DIA, GMD, GQM and WRT methods were compared for ideal test cases. The GQM was in good agreement with the exact WRT method while its medium resolution conjuration was ~10 times faster than WRT. The GMD was more than 50 times faster than GQM but it could not reproduce WRT results for slanting fetch condition. Two different packages named *ST3* and *ST6*, were employed for calculating the wind input and energy dissipation formulations over the Gulf of Mexico. The high quality ERA5 wind data from August to September in 2017 blended with Holland parametric model were used to run the wave model. The simulation period includes both fair weather condition and extreme events of Hurricanes Harvey and Irma. The performance of wave model using different nonlinear wave interaction terms was assessed against bulk wave parameters measured by *in-situ* buoys as well as altimeter-derived data by introducing a new error index. The general features of *in-situ* directional wave spectra were well captured by all DIA, GMD, GQM and WRT methods; however, the spectra produced by GMD and GQM were closer to the results by WRT method. Interestingly, the DIA method with calibrated whitecap dissipation term outperformed other methods in reproducing *in-situ* data (i.e. wave bulk parameters and wave spectra) during both fair weather and extreme events; indicating overfitting in the white capping or/and wind input terms in the wave model.

1. Introduction

WAVEWATCH-III (hereinafter WWIII) is a state-of-the-art, phase-averaged model which numerically solves the conservation of wave action equation:

$$\frac{DN}{Dt} = \frac{S_{tot}}{\sigma} \tag{1}$$

where N is the wave action equal to $\frac{E}{\sigma}$, in which E is the energy density and σ is angular frequency. The term S_{tot} on the right hand side of Eq. (1) represents several factors contributing in the wave evolution. In deep water, the energy transfer from wind (S_{in}), the nonlinear quadruplet wave-wave interaction (S_{nl}), and the dissipation due to white capping (S_{ds}) are the main factors in S_{tot} (Group WID 2016). Several packages are available in the WWIII for S_{in} and S_{ds}. In *ST3* package, which is based on WAM-Cycle4, the wind input is formulated as a function of $\frac{u_*}{C}$ in which u_* is friction velocity and C is phase speed velocity (Janssen, 1991). An iterative process is needed to include the feedback of wave-induced shear on the wind profile. The whitecap dissipation for *ST3* package is presented in Eq. (2). It includes C_{ds} parameter to tune the intensity of dissipation, and two weighted coefficients δ_1 and $\delta_2 = 1 - \delta_1$ to change its frequency distribution. Moreover, θ, $\overline{k}$, $\overline{\sigma}$, $\overline{\alpha}$ are wave direction, mean wave number, mean angular frequency and mean steepness respectively.

$$S\_ds(k,\theta) = C\_ds(\alpha^{-\wedge}2)\sigma^{-}[\delta\_1k \,/\, k^{-} + \delta\_2(k/k^{-})^{\wedge}2]N(k,\theta) \tag{2}$$

In the most recent formulation added to the WWIII model, called *ST6*, the wind input term includes the effect of opposing wind to wave as follows:

* Corresponding author.
E-mail address: Siadatmousavi@iust.ac.ir (S.M. Siadatmousavi).

https://doi.org/10.1016/j.apor.2022.103316
Received 27 April 2022; Received in revised form 29 July 2022; Accepted 11 August 2022
Available online 23 August 2022

$$w_1 = \max\left(0, \frac{U}{C}\cos(\theta - \theta_w) - 1\right)^2, w_2 = min\left\{0, \frac{U}{C}\cos(\theta - \theta_w) - 1\right\}^2 \quad (3)$$

$$w = w_1 - a_0 w_2 \quad (4)$$

where θ_w is wind direction, and U is wind velocity. The term -$a_0 w_2$ in Eq. (4) is called negative wind input which shows dissipation of waves by opposing wind (Donelan et al., 2006). In this study, a_0 is set to 0.09 (Liu et al., 2017). The wind speed should be scaled with friction velocity. To avoid overestimation in high frequencies, $32u_*$ is used following (Liu et al., 2019). The dissipation in *ST6* is presented as follows:

$$S_{ds}(k,\theta) = [T_1(k,\theta) + T_2(k,\theta)]N(k,\theta) \quad (5)$$

$$T_1(k) = a_1 A(k)\frac{\sigma}{2\pi}\left[\frac{\Delta(k)}{\widetilde{N}(k)}\right]^{p_1}, \ T_2(k) = a_2\int_0^k A(k)\frac{c_g}{2\pi}\left[\frac{\Delta(k)}{\widetilde{N}(k)}\right]^{p_2} dk \quad (6)$$

where $\Delta(k){=}N(k) - N_T(k)$, N_T is wave action threshold level, c_g is wave group velocity, σ is angular frequency, a_1 and a_2 are tuning parameters, $\widetilde{N}(k)$ is wave generic action density spectrum, and $A(k)$ is directional narrowness function, and $p_1{=}p_2{=}4$ are suggested values presented in the model. The T_2 term was added to general dissipation term T_1 to include the effect of long waves on the dissipation of short waves (Zieger et al., 2015).

The performance of wave models during severe meteorological events such as tropical cyclones (hereafter TC), hurricanes, and typhoons are of the utmost importance. The official season of hurricanes in the North Atlantic Ocean starts generally from June and ends in November. During the dominance of these extreme phenomena, high waves, flood, and storm surge cause costly devastations on infrastructures, oil and gas platforms, and coastal resorts at the U.S. East Coast and Gulf of Mexico (hereafter GOM).

Wind field in TCs is a compact low-pressure system like a vortex with counter-clockwise rotations (in the northern hemisphere) which evolves in time and space. The center of TCs experiences low wind speeds; however, intense winds are expected close to the eye. Wind speed is higher at the right-hand side of TCs where wind vectors are aligned with the translation speed leading to asymmetric wind field; hence stronger waves are expected on the right quadrants of a TC. In fact, more wave asymmetric features are expected due to the extended fetch than due to wind field (Young, 2006; Tamizi et al., 2021).

Esquivel-Trava et al. (2015) studied the spatial features of fourteen hurricanes passed over the Caribbean Sea and GOM. Their results showed complex wave spectra (bi and tri-modal) at a far distant region in front and rear quadrants. Moreover, peak wave direction generally deviates significantly from the wind direction except in the region with intense winds.

Due to the complexity of wind and wave field within TCs, wave spectra includes wind sea and swell components associated with local wind and radiated waves from the intense wind region. Wind seas are more aligned with the wind direction, and bi-modalities in frequency or direction was are expected. Uni-modal wave spectra similar to traditional fetch-limited wave spectrum such as JONSWAP have been attributed to study the role of nonlinear quadruplet wave-wave interaction in shape stabilizing of the wave spectrum (Young, 2006; Tamizi et al., 2021; Tamizi and Young, 2020). In fact the S_{nl} term is the most expensive one in a wave model. This term was not considered in wave simulations for decades because of the analytical difficulties of exact solution and the absence of suitable computational facilities; however, there have been intense endeavors for developing more accurate and faster methods within past four decades.

Moon et al. (2004) performed ideal test cases with different physical characters for hurricanes (e.g., translation speed, maximum wind speed, symmetric/asymmetric shape) using the WWIII model. Increasing the translation speed results in more developed, longer, and higher waves in the right-front quadrant, while younger, shorter, and lower waves are expected in the left-rear quadrant. The wave field under hurricane effects mostly depends on two factors: the distance relative to the hurricane center and the hurricane translation speed. Shih, Chen (Shih et al., 2018) conducted tide-surge-wave fully coupled model to provide potential risk maps for TCs induced waves along Taiwanese coasts. They showed the dependency of magnitude and spatial distribution of maximum significant wave heights on the TCs track and intensity.

The complexities of the rapidly evolving wind field during TCs as well as forcing physics deficiencies in wave models are two significant challenges for accurate wave simulations. Wind reanalysis data is sufficiently accurate for providing wind fields away from the center of the TCs, while parametric methods are better at regions close to the TC center; hence, the blend of wind reanalysis products and parametric methods could be feasible solution to enhance the quality of wind field forcing wave and circulation models (Chen et al., 2019; Hsiao et al., 2020). Siadatmousavi et al. (2011) calibrated WAM-Cycle4 in the SWAN model during Hurricane Dennis (2005) in the GOM. The spectrum evolution indicates that the calibrated whitecap dissipation term outperformed the default term for frequencies in the range of 0.12–0.17 Hz.

Liu et al. (2017) compared the performance of WWIII and UMWM models during Hurricane Ivan (2004) against buoy and remote sensing data. The simulations in WWIII model were performed using *ST2, ST3, ST4*, and *ST6* formulations. Statistical indices proved that the weakest performance in reproducing wave bulk parameters was obtained by UMWM and by *ST2* formulations in WWIII model; however, *ST3, ST4*, and *ST6* formulations provided accurate results. The misalignment of wind and peak wave directions is common under hurricane conditions. Wind sea and following swell occurs in the right-front quadrant while opposing swell prevails in the rear quadrants. Cross swell generally appears everywhere with moving outward relative to the hurricane center. The comparison with remote sensing data shows that the wave spectrum for wind sea and following swell is well predicted by the model, while all formulations overestimate the cross swell and opposing swell. This deficiency might be partially ameliorated by modifying S_{in} term in *ST6* formulation during cross and opposing swell conditions (Chen et al., 2019).

Hsiao et al., 2020 simulated the wave fields over the northwest shelf of Australia for seventeen TCs using WWIII model with default and calibrated values for *ST4* and *ST6* formulations. There was no single configuration to outperform others during all TCs. They showed the potential for improving the model results by inclusion of *ST6* with a more accurate calculation of S_{nl} term.

Chen et al., 2019 calibrated *ST3, ST4*, and *ST6* formulations in WWIII model for simulating Hurricane Ivan (2004). The *ST6* package with increased a_o and swell attenuation term was more suitable for buoys in the vicinity of the hurricane path, while TEST471 of *ST4* with increased β parameter led to better performance at far buoys and during fair weather conditions.

Hurricane impact on sea surface temperature, vertical mixing, and surface currents is inevitable; hence, sharing information between ocean and wave models could result in a more realistic sea state extimates (Chang et al., 2021; Chen et al., 2017). Sun, Perrie (Sun et al., 2018) considered wave-current interaction during extreme hurricanes along the US East Coast. Their results indicated that current alters wave height up to ±10% around hurricane swath. Current-induced refraction could result in a higher wave height at coastal regions (Sun et al., 2022). Abolfazli, Liang (Abolfazli et al., 2020) evaluated the climatology of wave height in the GOM for a 10-year period using coupled current and wave models. They concluded that current alters mean significant wave height up to ±15%. In addition, in the case where loop current extended northward in the GOM, wave height modulation by current reaches to ±35%. Reducing wave height was appeared in the southwestern GOM, while increasing wave height was obvious over the northeastern GOM coasts.

In most of previous studies, some buoys have been used for model assessment while in this study, a new combined error is introduced, which includes buoys and altimeter data. The model calibration is performed based on both energy content (which affect H_s) and energy distribution (which affects T_m) for *ST3* and *ST6* packages. Moreover, the Gaussian Quadrature Method (GQM) as an accurate method for S_{nl} estimation in deep water, was implemented in WWIII model for the first time. Its performance was checked for test cases first, and then it was combined with depth scale formula to be used for simulation of wave within the GOM. Section 2 reviews the features of well-known methods for calculating S_{nl} term in WWIII model. Section 3 describes the study area and available measurements as well as input data for wave model. Section 4 contains details of the methodology for model calibration with new introduced error parameter and the model setup. The comparison of wave model results using different S_{nl} terms with buoys and altimeter data during both fair weather and hurricane conditions was presented in Section 5. This section was followed by summary and conclusion in Section 6.

2. Quadratic nonlinear wave interaction in WWIII

2.1. WRT

The full mathematical formulation of the nonlinear quadruplet wave-wave interaction (S_{nl}) is as follows (Hasselmann, 1962).

$$\frac{\partial n_1}{\partial t} = \int\int\int G\left(\vec{k}_1, \vec{k}_2, \vec{k}_3, \vec{k}_4\right) \times \delta\left(\vec{k}_1 + \vec{k}_2 - \vec{k}_3 - \vec{k}_4\right) \times \delta(\sigma_1 + \sigma_2 - \sigma_3 - \sigma_4) \times [n_1 n_3 (n_4 - n_2) + n_2 n_4 (n_3 - n_1)]\, d\vec{k}_2 d\vec{k}_3 d\vec{k}_4 \tag{7}$$

in which G is the coupling coefficient which was first presented and simplified for deep water condition (Hasselmann, 1962; Webb, 1978). It was later extended to shallow water (Herterich and Hasselmann, 1980). Two delta functions in Eq. (7) ensure that the resonant interaction occurs only when $\vec{k}_1 + \vec{k}_2 = \vec{k}_3 + \vec{k}_4$ and $\sigma_1 + \sigma_2 = \sigma_3 + \sigma_4$ where σ_i, $\vec{k}_i$ and n_i are radian frequency, wave number vector and action density spectrum, respectively. The dispersion equation $\sigma_i^2 = g k_i \tanh(k_i h)$ must hold in which g and h are gravity acceleration and water depth.

The given $\vec{k}_1$ and $\vec{k}_3$ the $\vec{k}_2$ and $\vec{k}_4$ trace out parallel 'egg-shaped' closed curves (Webb, 1978). Webb (1978) and Chang et al., 2021 tried to eliminate delta functions and transformed six-fold integration in Eq. (7) to a simpler integration along egg-shaped loci which can be expressed as follows:

$$T\left(\vec{k}_1, \vec{k}_3\right) \oint G(s) \times \underbrace{[n_1 n_3 (n_4 - n_2) + n_2 n_4 (n_3 - n_1)]}_{N} \times J(s) \times ds \approx \sum_{i=1}^{i=N_s} G(s_i) \times N(s_i) \times J(s_i) \times \Delta s_i \tag{9}$$

In Eq. (9), $J = |\vec{C}_{g,2} - \vec{C}_{g,4}|^{-1}$ is the Jacobian term with $\vec{C}_{g,2}$ and $\vec{C}_{g,4}$ denoting the group velocities at $\vec{k}_2$ and $\vec{k}_4$ respectively, and N_s is the number of points on loci. This method is known as Webb-Resio-Tracy 'WRT' method which has been implemented as a portable Fortran module for third generation model by Chen et al., 2017.

The main part of WRT method is determining the distribution of discrete points on $\vec{k}_2$ and $\vec{k}_4$ loci, which has been handled by Tracy and Resio (Chang et al., 2021) using a radial method. To remedy the non-uniform distribution of points on the locus in shallow waters, the polar method was suggested (Sun et al., 2018). Adaptive polar, an iterative method base on polar method, results in a more even distribution of points on the locus, and has been used in WWIII (Sun et al., 2018).

2.2. DIA

Hasselmann et al. (1985) devised an approximate solution of S_{nl} with selecting only one representative interaction configurations among all possible ones. The Discrete Interaction Approximation (DIA) was developed as a fast and practical method to calculate S_{nl}. Due to its high efficiency, DIA has been the default method in the third-generation wave models such as WAM, SWAN, WWIII, and TOMOWAC. The representative four wave components in this method are as below:

$$\begin{cases} \vec{k}_1 + \vec{k}_2 = \vec{k}_3 + \vec{k}_4 \\ \sigma_1 = \sigma_2 \\ \sigma_3 = (1+\lambda)\sigma_1 \\ \sigma_4 = (1-\lambda)\sigma_1 \end{cases} \tag{10}$$

where λ is equal to 0.25. The contribution of described four wave components in S_{nl} term for DIA method is computed as:

$$\begin{pmatrix} \delta S_{nl,1} \\ \delta S_{nl,2} \\ \delta S_{nl,3} \end{pmatrix} = \begin{pmatrix} 2 \\ -1 \\ -1 \end{pmatrix} Cg^{-4} f_1^{11} \left[F_1^2 \left(\frac{F_3}{(1+\lambda)^4} + \frac{F_4}{(1-\lambda)^4} \right) - 2\frac{F_1 F_3 F_4}{(1-\lambda^2)^4} \right] \tag{11}$$

in which $F_i(f_i, \theta_i)$ denotes the spectral energy density, $\delta S_{nl,i} = \delta S_{nl}(f_i, \theta_i)$ represents the contribution to S_{nl} term, and $C = 3 \times 10^7$ is the constant coefficient recommended by Hasselmann et al. (1985) but varies between 1×10^7 and 3×10^7 in WWIII model when different packages for S_{in} and S_{ds} are employed.

The S_{nl} term of DIA was originally developed for deep water condition. A scale factor in the form of $S_{nl}^{shallow} = R \times S_{nl}^{deep}$ is assumed as follows (Komen et al., 1994):

$$R(x) = 1 + \frac{5.5}{x}\left(1 - \frac{6}{7}x\right) e^{\left(-\frac{5}{4}x\right)} \tag{12}$$

in which x is equal with $0.75 k_m h$ where k_m denote the mean wave number.

Resio and Perrie (2008) and Perrie et al. (2013) compared the obtained S_{nl} term for JONSWAP spectrum with different considered values for peak enhancement parameter (γ=1, 3.3, and 7) against the exact solution. For fully developed spectrum (γ=1), the positions of positive and negative lobes were close to positions from the exact solution, but DIA overestimated (underestimated) positive (negative) lobes; hence, more dissipation and more wind input energy were needed on the forward and rear faces of the spectrum, respectively. Simulated S_{nl} term with DIA started to deviate from the exact solution as γ parameter increased. Furthermore, spurious positive and negative lobes were appeared on the rear face of the spectrum.

In deep water condition, S_{in}, S_{ds}, and S_{nl} mainly control the wave spectrum evolution, and their balance in equilibrium range ensures the f^{-4} spectral form (Resio and Perrie, 1989; Young and Van Vledder, 1993). Ardag and Resio (2019) used the DIA method in pure nonlinear interaction condition (S_{in}=S_{ds}=0) for JONSWAP spectrum and showed gradual deviation of the high frequency part of the spectrum from f^{-4} spectral form. To compensate this deficit, unrealistic wind input and whitecap tuning values would be selected in the calibration process of the model.

Rogers and Van Vledder (2013) performed a 10-days simulation for the Michigan Lake. They reported more accurate results when exact solution for S_{nl} was used instead of DIA method. Moreover, the frequency spectrum obtained with the exact solution for S_{nl} term was narrower than with DIA method. The overprediction of energy transfer to frequencies below the spectral peak would result in broad spectra when DIA was applied.

2.3. GMD

Increasing the number of representative configurations for interaction was a strategy to improve the accuracy of DIA. The Extended Discrete Interaction Approximation (EDIA) method was proposed Hashimoto and Kawaguchi, 2001) based on Eqs. (10), ((11) by considering six representatives. The Multiple Discrete Interaction Approximation (MDIA) method (Sun et al., 2022) uses more than one representative configurations. The four wave components in the resonant interaction should satisfy the following equations:

$$\begin{cases} \vec{k}_1 + \vec{k}_2 = \vec{k}_3 + \vec{k}_4 \\ \sigma_1 = (1+\mu)\,\sigma \\ \sigma_2 = (1-\mu)\,\sigma \\ \sigma_3 = (1+\lambda)\,\sigma \\ \sigma_4 = (1-\lambda)\,\sigma \end{cases} \tag{13}$$

This method can be reduced to DIA if μ=0 and only one representative interaction was used. Three unknown constants μ, λ, and C for each representative configuration were obtained by an optimization process (Sun et al., 2022, Tolman, 2003).

The Generalized Multiple Discrete Interaction Approximation (GMD) also applies a resilient set of representative four wave components. It adds one more free parameter θ_{12} (θ_2=$\theta_1 \pm \theta_{12}$) to Eq. (13) in order to define the angle between $\vec{k}_1$ and $\vec{k}_2$. It outperformed DIA because: (1) multiple representative quadruplets were applied; (2) individual quadruplets in GMD were estimated at actual depth without need to use Eq. (12). The S_{nl} term in GMD can be expressed as follows:

$$\begin{pmatrix} \delta S_{nl,1} \\ \delta S_{nl,2} \\ \delta S_{nl,3} \\ \delta S_{nl,4} \end{pmatrix} = \begin{pmatrix} -1 \\ -1 \\ 1 \\ 1 \end{pmatrix} \left(\frac{1}{n_{q,d}} C_{deep} B_{deep} + \frac{1}{n_{q,s}} C_{shal} B_{shal} \right) \left[\frac{C_{g,1}F_1}{k_2\sigma_2} \frac{C_{g,2}F_2}{k_2\sigma_2} \left(\frac{C_{g,3}F_3}{k_3\sigma_3} + \frac{C_{g,4}F_4}{k_4\sigma_4} \right) - \frac{C_{g,3}F_3}{k_3\sigma_3} \frac{C_{g,4}F_4}{k_4\sigma_4} \left(\frac{C_{g,1}F_1}{k_2\sigma_2} + \frac{C_{g,2}F_2}{k_2\sigma_2} \right) \right] \tag{14}$$

$$B_{deep} = \frac{k^{4+m}\sigma^{13-2m}}{(2\pi)^{11} g^{4-m} C_g^2} \quad B_{shal} = \frac{k^{11}g^2}{(2\pi)^{11} C_g} \, (kh)^n \tag{15}$$

where C_{deep} and C_{shal} are constants coefficients, $n_{q,d}$ and $n_{q,s}$ are the number of representatives with deep and shallow scaling, B_{deep} and B_{shal} are scaling functions for weak and strong interactions, and m and n are tunable parameters. To obtain the unknown parameters, the genetic optimization technique was employed (Tolman and Grumbine, 2013; Tolman, 2013). This method is available in the WWIII model.

2.4. GQM

Lavrenov (2001) considered deep water condition and presented S_{nl} in terms of the variance density spectrum as follows:

$$\frac{\partial F_1}{\partial t} = \int_{\sigma_2=0}^{+\infty} \int_{\theta_2=0}^{2\pi} \times \int_{\sigma_3}^{\frac{\sigma_a}{2}} 2 \frac{\sigma_a^4 G}{\sigma_2\sigma_3\sigma_4} \frac{F_3F_4\left(F_1\sigma_2^4 + F_2\sigma_1^4\right) - F_1F_2\left(F_3\sigma_4^4 + F_4\sigma_3^4\right)}{\sqrt{\widetilde{B}_0(\varepsilon_a, w_3)\widetilde{B}_1(\varepsilon_a, w_3)\widetilde{B}_2(\varepsilon_a, w_3)}} d\sigma_2 d\theta_2 d\sigma_3 \tag{16}$$

where σ_a=$\sigma_1 + \sigma_2$, ε_a=$\frac{2gk_a}{\sigma_a^2}$, k_a is the magnitude of $\vec{k}_a$=$\vec{k}_1 + \vec{k}_2$, and w_3=$\frac{\sigma_3}{\sigma_a}$. The non-dimensional functions $\widetilde{B}_0$, $\widetilde{B}_1$, and $\widetilde{B}_2$ can be found as follows:

$$\widetilde{B}_0 = \left[\frac{1}{2}\left(1+\frac{\varepsilon_a}{2}\right) - w_3\right]\left[\left(w_3 - \frac{1}{2}\right)^2 + \frac{1}{4}(1+\varepsilon_a)\right] \tag{17}$$

$$\widetilde{B}_1 = w_3 - \frac{1}{2}\left(1 - \frac{\varepsilon_a}{2}\right) \tag{18}$$

$$\widetilde{B}_2 = \left(w_3 - \frac{1}{2}\right)^2 - \frac{1}{4}(\varepsilon_a - 1) \tag{19}$$

The denominator of Eq. (16) is zero for some θ values, and Gaussian quadrature methods were used to handle the singularities (Lavrenov, 2001; Gagnaire-Renou, 2009). The integration over σ_3 was divided into two segments and calculated using Gauss–Legendre and Gauss–Chebyshev methods. The integrations over the θ_2 and σ_2 were obtained by Gauss–Chebyshev and first order trapezoidal methods, respectively. This developed method is known as Gaussian Quadrature Method (GQM).

The accuracy of GQM is highly dependent on the number of points used for integrations. There are three sets of resolutions: (1) fine resolution including (26,16,12) points; (2) medium resolution including (14,8,8) points; and (3) rough resolution (11,6,6) including points for σ_2, θ_2, and σ_3 integrations. Applying rough resolution for JONSWAP spectrum led to unsatisfactory results. Due to more computational cost with increasing the resolution, and sufficient proximity of the medium resolution results to the exact solution, the medium resolution has been recommended in previous researches (e.g. Gagnaire-Renou et al., 2010; Gagnaire-Renou et al., 2011).

Benoit (2007) applied DIA, MDIA, and GQM in the TOMWAC model for a single grid point simulation. The simulated wave height (H_s), peak period (T_p), and directional width for DIA were higher than results from MDIA and GQM. Also, some secondary spurious peaks have been observed when MDIA was used. Moreover, frequency distribution for MDIA was narrower than other methods. Benoit (2005) evaluated the DIA, MDIA, GQM, and some diffusion-type methods for the JONSWAP spectrum with γ=3.3 and showed superiority of the GQM.

2.5. Preliminary GQM validation in WWIII model

The GQM code was added to the *W3SNLXMD* module in WWIII model. Before applying this method for a real condition, the code was used for some ideal cases as presented in this section. For all tests, deep water condition was assumed. Moreover, the spectral space was discretized into 36 directions and 50 frequencies in the range of 0.04–1 Hz, with a geometrical incremental rate of 1.07.

2.5.1. Duration-limited tests

For the first duration-limited test case, ure nonlinear interaction was performed in which only S_{nl} was kept active for wave evolution. The JONSWAP wave spectrum was used to generate waves with H_s=0.1 m, T_p=3 s, and three values of 1, 3 and 5 for γ parameter. The directional wave spectrum were produced by applying the Mitsuyasu-Hasselman spreading function (Hasselmann et al., 1985). The estimated S_{nl} terms using DIA, GMD, three resolutions for the GQM, and WRT method were compared in Fig. 1. The S_{nl} term from DIA was multiplied by 0.2 to provide consistent magnitudes with other methods. The rough resolution of GQM led to some fluctuations in the rear face of the spectrum but the medium resolution was in good agreement with GMD and WRT methods. All GQM alternatives outperformed DIA method. For γ=1 the position of positive and negative lobes of DIA coincided with other methods but with increasing γ parameter, some spurious positive and negative lobes appeared in the high-frequency part of the spectrum as mentioned before in Section 2.2.

The directional spectrum from different methods are designated in Fig. 2. The S_{nl} term from DIA method was broader than exact solution. In addition, negative lobes for the DIA method were much wider than other methods (see also Fig. 1). With increasing γ parameter, DIA yielded two

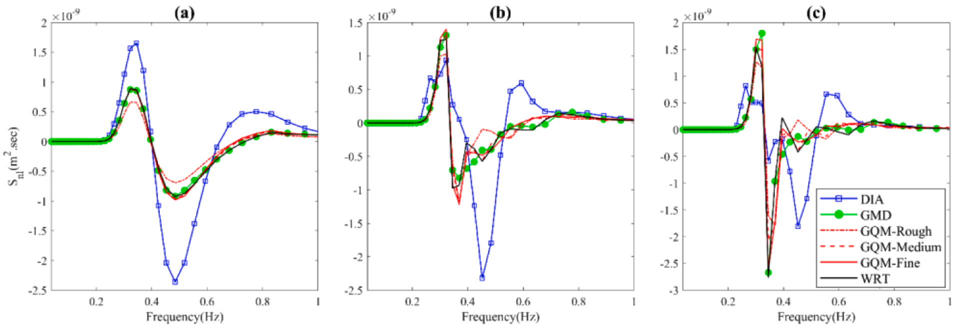

Fig. 1. One-dimensional S_{nl} terms for the JONSWAP spectrum with (a) $\gamma = 1$; (b) $\gamma = 2$; and (c) $\gamma = 3$ using different methods. For the consistency of the magnitude order among different methods, DIA-derived values were multiplied by 0.2.

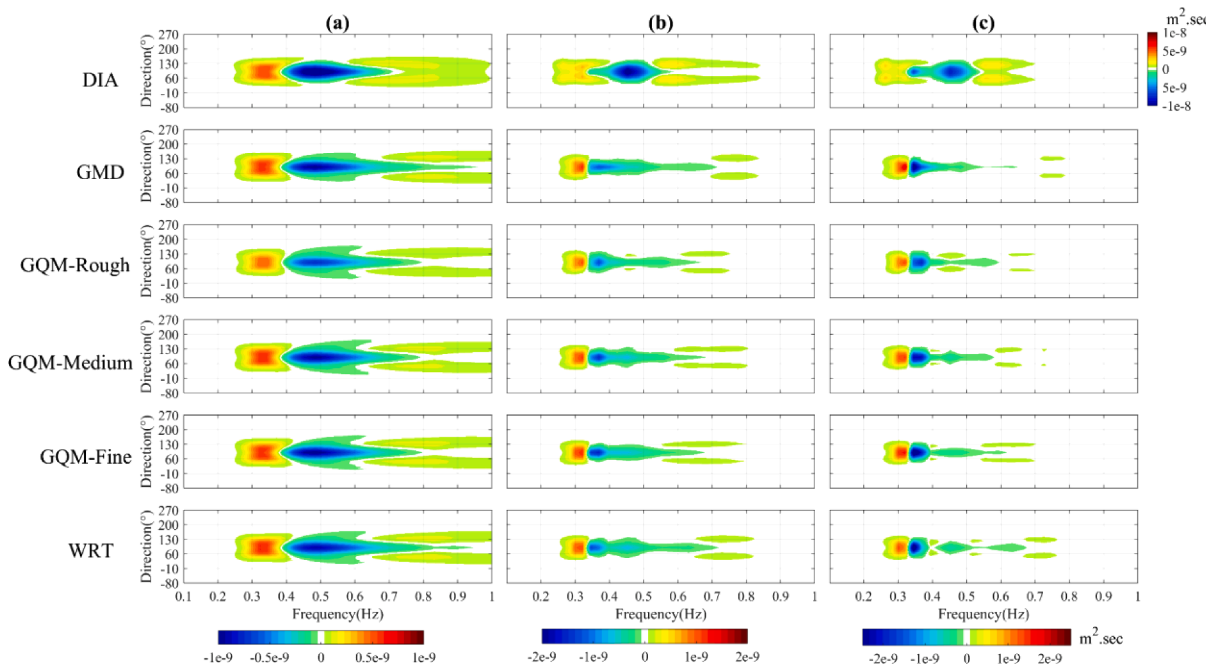

Fig. 2. Two-dimensional S_{nl} term for JONSWAP spectrum with (a) $\gamma = 1$, (b) $\gamma = 2$, and (c) $\gamma = 3$. Colorbar for DIA method is provided at the outer part of the first row, and for other methods is presented at the lowest end of each column. (For interpretation of the references to color in this figure legend, the reader is referred to the web version of this article.)

distinct positive lobes in low frequency part of the spectrum which was not consistent with exact WRT method. In other words, spurious bi-modality in direction (at low frequencies) and high directional spreading are expected when DIA is applied in simulations. The results from medium and fine resolutions GQM were in accordance with WRT method. Since the medium resolution alternative was 6–8 fold faster than the fine resolution one, it was used in this study hereafter. Similar to GQM, GMD method successfully reproduced S_{nl} results estimated by WRT method.

The second test case for the duration-limited condition was conducted in WWIII model according to test case B of Benoit (Benoit, 2007). In this test case, the wind direction has three stages: (1) wind direction is 90° for time period from t = 0 to 8 h; (2) wind veers suddenly to 30° at t = 8 h and remains with no change until t = 18 h; (3) the wind direction abruptly changes to 120° at t = 18 h and stays invariant until t = 96 h. The wind velocity is equal to 20 m/s during entire simulation. The initial wave spectrum of the JONSWAP type with H_s=0.1 m, T_p=3 s, and γ=3 was used. The *ST6* formulation with default values, according to Liu et al. (2019) was applied for S_{in} and S_{ds}.

The time series of H_s, T_p, directional spreading, and mean wave direction are shown in Fig. 3. The DIA resulted in higher H_s and T_p than other methods. At the early stages of the wave growth, the results from GMD, GQM and WRT methods were similar; however, as time passed, H_s and T_p from GMD method approached to results from DIA method. In accordance with results of previous test, the DIA had high directional spreading, while the lowest values were obtained by GMD. There was a good agreement between GQM and WRT methods in this case. In terms of mean wave direction, all methods were similar except DIA. Although not shown here, the directional wave spectra from all methods showed that the high-frequency part of the spectrum is more aligned with change in wind direction (Young et al., 1987).

The CPU time for this single grid point test case was provided in Table 1 when a personal computer with Intel® core^{TM} i7-3370 processor was employed. As expected, the DIA method was the fastest method. The GMD method was ~4.5 times more expensive than DIA. The GQM method was more than 200 times slower than DIA; however, it was 1 order of magnitude faster than using WRT method.

2.5.2. Fetch-limited test

Uniform constant wind speed of 20 m/s was considered over one-dimensional domain of 8750 km length. The simulation was conducted for 72 h in WWIII model. The *ST6* formulation with default values

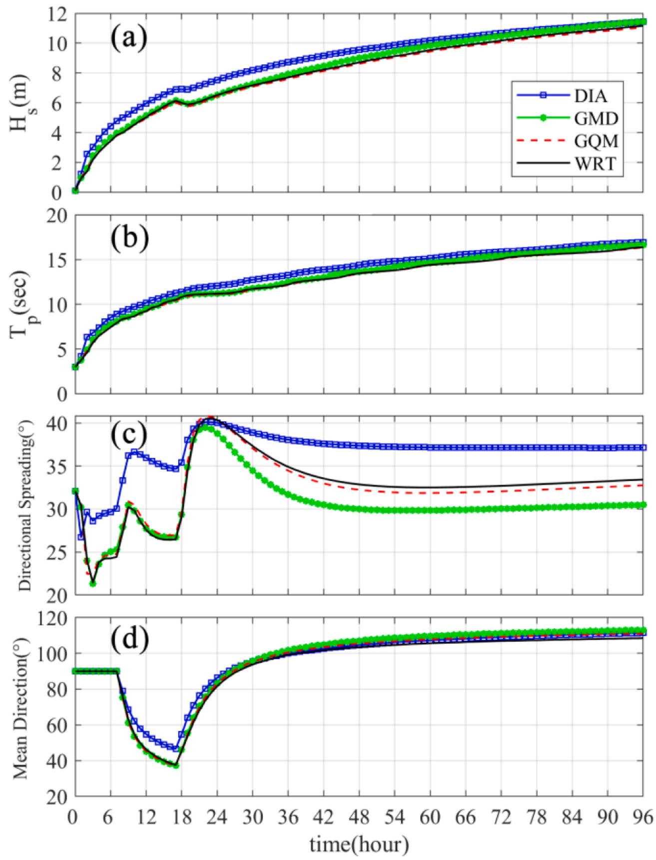

Fig. 3. Time series of (a) H_s, (b) T_p, (c) directional spreading, and (d) mean wave direction using different methods for S_{nl} term in the second test.

Table 1
The CPU time consumption of different applied methods for S_{nl} term in WWIII model.

Method	DIA	GMD	GQM	WRT
CPU time (Second)	4.68	21.21	1053.99	10871.74

were used. A recently introduced values for tuning coefficients of GMD for *ST6* package was used according to Liu et al. (2019). The linear wave growth is important at the early stages of wave development and considered in the model according to Cavaleri and Rizzoli (1981).

Two relations proposed by Kahma and Calkoen, (1992) (hereafter KC1992), and Romero and Melville, (2010) (hereafter RM2010) were used to assess the model performance in this fetch-limited test as shown in Fig. 4. In this figure, non-dimensional fetch length, energy and peak frequency are $X_*=\frac{gX}{u_*^2}$, $\varepsilon_*=\frac{H_s^2 g^2}{16u_*^4}$ and $\nu_*=\frac{f_p u_*}{g}$, respectively; where X is fetch length, g is gravitational acceleration and u_* is friction velocity. The saturation level of the wave growth, which happens at long fetches, can be evaluated against the Pierson–Moskowitz limits (Komen et al., 1994). The predicted H_s using DIA method was greater than predictions of 'KC1992', and 'RM2010' relations; even at the saturation level. Unlike DIA, all GMD, GQM, and WRT methods closely followed measured data and the Pierson-Moskowitz limit. Simulated peak frequency by all methods was in agreement with measured data at low fetches; however, slight underestimation occurred when DIA method was incorporated. With increasing the fetch, the simulated peak frequency values started to deviate from measurements. Non-dimensional wave height and peak frequency predicted by GMD and GQM mimicked the WRT results closely.

2.5.3. Slanting fetch-limited test

The wave energy and peak frequency in fetch-limited condition strongly depends on wind obliquity. The wave is more energetic and developed in slanting fetch condition than in situation where wind blows perpendicular to the shoreline (Gagnaire-Renou, 2009). In this section, a slanting fetch-limited test case was conducted with uniform constant wind speed of 10 m/s with obliquity of 20°. The one-dimensional domain of length 1000 km was used for simulations. The model results using different methods was presented in Fig. 5. Two setups were considered for GMD method: (1) GMD-G35d; the original deep water setup of G35d (Tolman, 2013); (2) GMD-Liu; recently recalibrated setup by Liu et al. (2019) for *ST6* package which was used also in Sections 2.5.1 and 2.5.2 for previous ideal cases.

It is clear from Fig. 5a that the DIA method resulted in higher normalize energy (i.e. H_s) along fetch than other methods while GQM and GMD-Liu resulted in lower wave energy at low fetches. The GQM closely followed the WRT results as fetch increased, but it underestimated the saturation level. Estimated saturation level by GMD-Liu is the same as WRT method. Predicted energy by GMD-G35d is in more agreement with WRT at small fetches; however, it follows the trend of DIA at long fetches. It is inferable that the GQM successfully resembled predicted H_s by GMD-Liu and WRT methods.

Unlike wave energy, the patterns of normalized peak frequency shown in Fig. 5b were not similar for methods. It is obvious that the GQM accurately reproduced estimated peak frequency by WRT method,

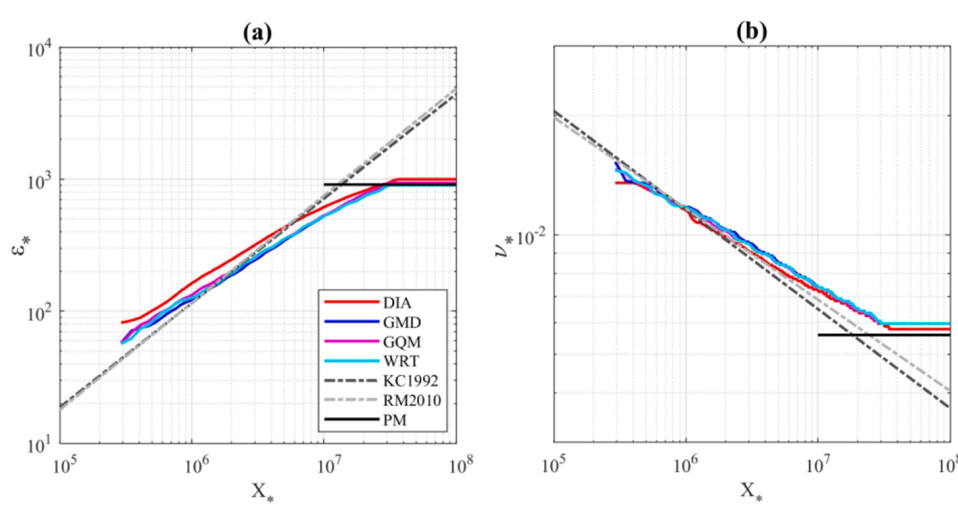

Fig. 4. Simulated non-dimensional (a) wave height and (b) peak frequency for fetch-limited condition. Both horizontal and vertical axes are in logarithmic scale.

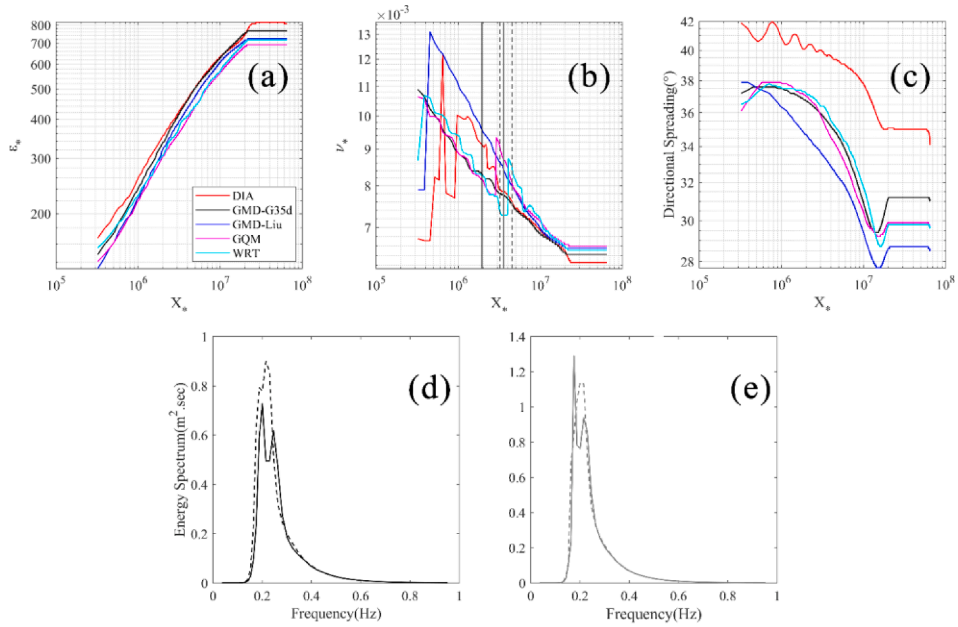

Fig. 5. Simulated non-dimensional (a) wave height and (b) peak frequency, (c) directional spreading for slanting fetch-limited condition. In (a–c) both horizontal and vertical axes are in logarithmic scale. (d) One-dimensional wave spectra by GQM method at two selected sections before and after sharp change in peak frequency shown in panel b. (e) is the same as (d) but for WRT method.

except the jump pattern which appeared at slightly smaller fetch for GQM. The agreement of GQM and GMD-G35d is remarkable before the jump, while obtained peak frequency by GQM or WRT was higher than that of GMD-G35d after the jump.

Directional spreading by all methods was compared in Fig. 5c. Estimated directional spreading by GQM and GMD-G35d closely mimicked the results of the WRT method, while DIA method severely overestimated the directional spreading. Moreover, GQM outperformed GMD-G35d at long fetches. Note that the narrowest wave spectrum was produced by GMD-Liu.

To scrutinize the reason for the jump in the normalized peak frequency shown in Fig. 5b for GQM and WRT methods, the one-dimensional wave spectra at two fetches before and after the jump were presented in Fig. 5d. The bi-modality is obvious before the jump which indicates the dominance of swell waves, while after the jump, the wave spectrum is unimodal and sea waves control the wave growth. In general, the quality and quantity aspects of simulated peak frequency by GQM method was the closest one to the WRT method. In addition, the new set of calibration presented in Liu et al. (2019) for *ST6* package was not successful in reproducing the peak frequency in this test.

3. Study area and model setup

3.1. Model domain and available data

The model domain in this study covers GOM from -98W to -79W and from 18N to 31.5N. It is a semi-enclosed basin with a mixture of intermediate and shallow waters over the continental shelf and extremely deep water (more than 1000 m) at the middle part. Several strong hurricanes generated at low latitudes in the North Atlantic Ocean had passed over GOM. Warm loop current in the GOM intensifies the hurricane strength before its landfall. This could result in extreme events such as high waves, storm surges, and coastal flooding in coastal regions. There is a host of NDBC (National Data Buoy Center) buoys in the GOM which provides wave spectrum, bulk parameters, and meteorological data at different places. Beside the frequency spectrum in the range of 0.02–0.485 Hz, most of these buoys provide few directional parameters which can be used with the Longuet–Higgins method to extract directional wave spectrum (Earle et al., 1999).

In this study, the available buoys were classified into three groups regarding their depth: (1) NDBC buoys 42001, 42002, and 42055 in which water depth was greater than 1000 m (hereinafter deep water buoys); (2) NDBC buoys 42039 and 42040 in which water depth was in the range of 100–1000 m (hereinafter intermediate water buoys); (3) NDBC buoys 42012, 42019, 42035, 42036 with water depth less than 100 m (hereinafter shallow water buoys). The study area and the location of selected buoys are shown in Fig. 6.

The altimeter data provided by Australian Ocean Data Network (AODN) were also retrieved from https://portal.aodn.org.au to evaluate the quality of available wind data and the model assessment. This dataset composed of wind velocity and H_s along 14 satellite tracks (Ribal and Young, 2019). The model data were then interpolated spatially and temporally over satellite track points. Following (Beyramzadeh et al., 2021), a simple filter was applied to extract independent data.

3.2. Input data

The bathymetry data was extracted from ETOPO1 dataset which was a 1-arc min global relief model of the earth surface (Amante and Eakins, 2009). The data is available via https://www.ngdc.noaa.gov/mgg/global/global.html. The isobaths in the GOM were shown in Fig. 6.

Hourly boundary conditions at the lower-right part of the domain were extracted in the form of directional wave spectra from a global wave modeling. A regular rectangular grid of $1.25^{\circ} \times 1^{\circ}$ resolution was employed for the global WWIII model following (Zieger et al., 2015; Siadatmousavi et al., 2016).

Oceanic currents affect the wave field because relative wind velocity should be imposed in wave model; Also the advection terms in the wave action equation (Eq. (1)) should be modified to account for wave modulation by currents (Group WID 2016). In this study, ocean current from HYCOM+NCODA Global $\frac{1}{12^{\circ}}$ dataset was used following (Fan and Rogers, 2016).

The reanalysis hourly wind data of ERA5, with 0.25° spatial resolution, were applied in all simulations. The data were accessible via http

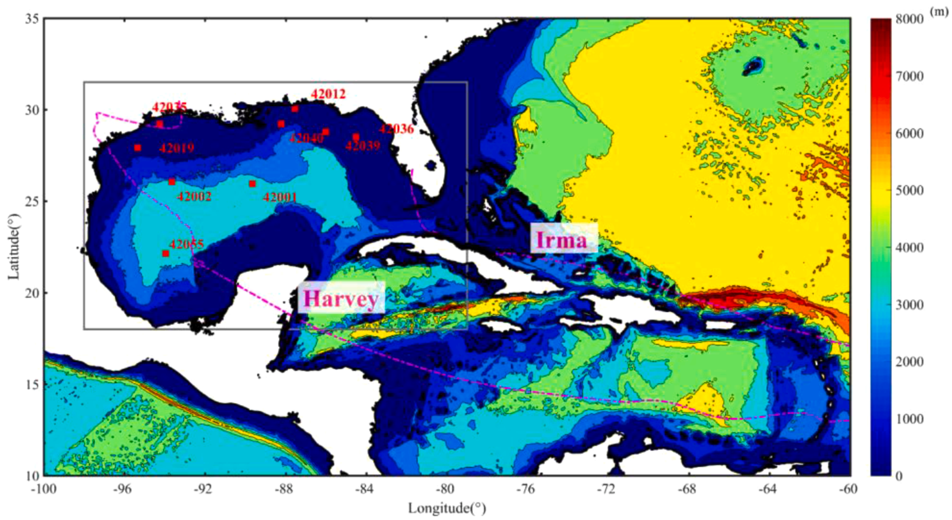

Fig. 6. The Study area, locations of NDBC buoys, and isobaths. The solid grey box is the study area. Solid red squares are 9 selected NDBC buoys. The west and east dash-dotted magenta lines present the path of Hurricanes Harvey and Irma, respectively. (For interpretation of the references to color in this figure legend, the reader is referred to the web version of this article.)

s://cds.climate.copernicus.eu. To improve the resolution close to the hurricane eye, parametric hurricane-induced wind velocity was generated and blended with ERA5 data within 3° around the hurricane center. The weight of ERA5 wind vector increased linearly from 0 to 1 as the distance from the center of hurricane increased from 2 to 3°. In the transition region weighted linear interpolation with respect to distance from hurricane center was used. Kalourazi et al. (2020) precisely evaluated different parametric methods for strong hurricanes within GOM and showed superior performance of the Holland et al. (2010) model. One of the vital parameters for presenting hurricane radial wind velocity with parametric method is R_{max}. They suggested to use fourth-order polynomial to find variable R_{max} around the hurricane center according to Xie et al. (2006). The same configuration was used here to present the hurricane radial wind velocity in the vicinity of the hurricane center. The hurricane physical parameters such as the position of hurricane center, the direction of hurricane translation, V_{max} (the maximum wind speed), V_m (translation speed), R_{34}, R_{50}, R_{64} (the radius in which the wind velocities were 34, 50, 64 kt), and central pressure were obtained from National Hurricane Center.

In Fig. 7, ERA5 wind data were evaluated against altimeter and NDBC buoys data for the period from 1 August to 15 September 2017. This period includes both fair weather condition as well as occurrence of two destructive Hurricanes Harvey and Irma. The Harvey tropical system approached the GOM on 21 August. During the next three days, it intensified and became a hurricane early on 24 August. It reached to category 3 on 25 August at the middle Texas coast and strengthen to

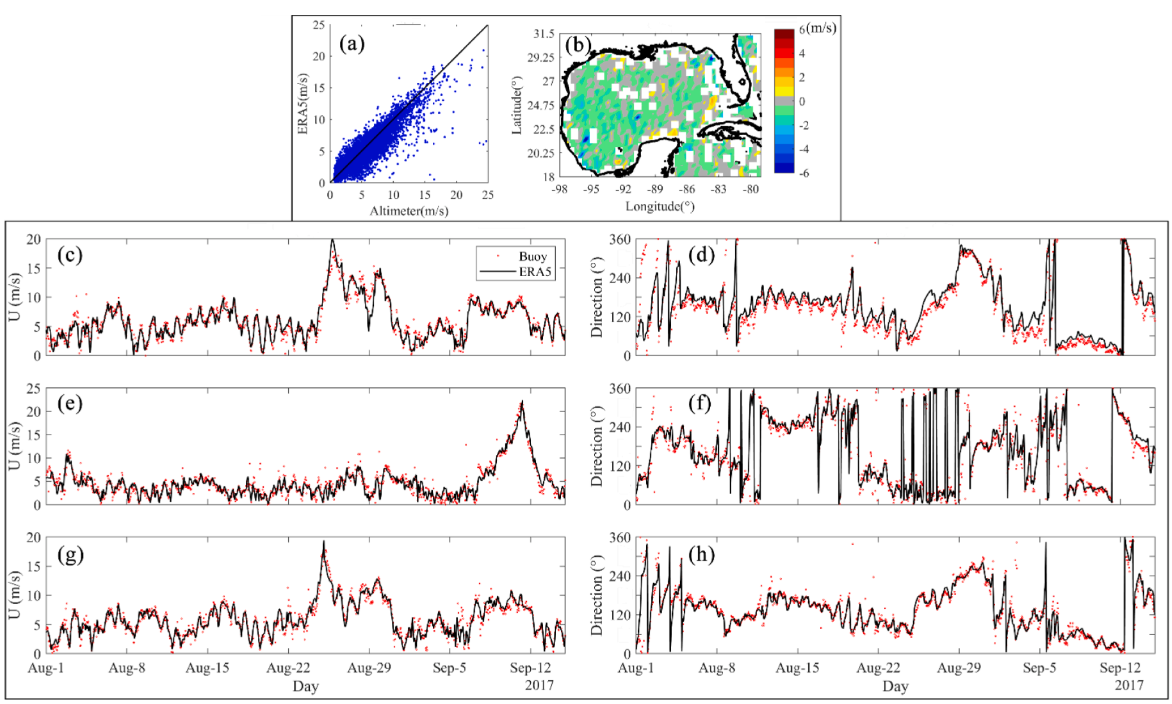

Fig. 7. (a) the scatterplot of ERA5 wind data vs AODN altimeter wind velocity for the period from August to September 2017; (b) the mean bias of ERA5 against AODN altimeter data. In lower solid black box, time series of ERA5 wind data were compared against NDBC data. In each row, left/right column relates to wind speed/wind direction. The data in panel (c–d) were for NDBC 42019; (e–f) for NDBC 42036; and (g–h) for NDBC 42002.

category 4 status on 26 August. It stayed as TC and depression status until it left the GOM on 31 August. Hurricane Harvey in its most severe status experienced the central pressure of 937 mbar and V_{max} of 115 knots. Hurricane Irma made 7 landfalls in its journey. Although Irma weakened to category 2 after its landfall in Cuba, it intensified to category 4 when moved over warm loop current through the Florida Strait. The maximum wind speed of the Hurricane Irma was 155 knots occurred on 6 September, and the associated central pressure was 914 mbar (Abdolali et al., 2021). The tracks of these two hurricanes were shown in Fig. 6.

NDBC buoys 42019 and 42001 (panels c and g in Fig. 7) clearly experienced Hurricane Harvey from 22 to 30 August, while NDBC buoy 42036 (panel e in Fig. 7) records high speed of Hurricane Irma from 8 to 12 September. It is clear that ERA5 slightly underestimated altimeter wind velocity (shown in panel a); however, there was acceptable agreement with NDBC buoys data.

4. Method

4.1. Model setup

The computational domain for WWIII model was a discretized with $0.08^{\circ} \times 0.08^{\circ}$ from −98W to − 79W in longitude and from 18N to 31.5N in latitude. The spectral domain consisted of 30 frequencies with geometrical distribution in the range of 0.04–0.64 Hz and 36 directions with 10° step. Unless it is specified, the DIA method was used for calculating the S_{nl} term. The maximum global time step, the spatial and spectral time steps and source term time step were set to 180, 90, 180 and 30 s, respectively. The depth-induced wave breaking was included in the model according to the method proposed by Battjes and Janssen (1978). The bottom friction (S_{bot}) was considered in the model using the JONSWAP method (Hasselmann et al., 1973) with its tuning coefficient equal to $-0.038\,\mathrm{m}^2\mathrm{s}^{-2}$ was set in WWIII model according to Zijlema et al. (2012), Alipour et al. (2021).

4.2. Model calibration and error indices

Three deep water buoy stations (42001,42002,42055) were used for model calibration. Two wave bulk parameters H_s and T_m simulated by both *ST3* and *ST6* packages in WWIII model were compared with deep water buoys from 1 August to 15 September 2017.

Three statistical indices of normalized mean bias (*NMB*), scatter index (*SI*) and normalized root mean square error (*HH*) were used for model assessments. In the following equations, M_i and O_i are modeled and observed data respectively, and N is the total number of data.

$$\boldsymbol{NMB} = \frac{\sum(\boldsymbol{M}_i - \boldsymbol{O}_i)}{\sum \boldsymbol{O}_i} \tag{20}$$

$$\boldsymbol{SI} = \frac{\sqrt{\frac{1}{N}\sum(\boldsymbol{M}_i - \boldsymbol{O}_i)^2}}{\overline{\boldsymbol{O}}} \tag{21}$$

$$\boldsymbol{HH} = \sqrt{\frac{\sum(\boldsymbol{M}_i - \boldsymbol{O}_i)^2}{\sum \boldsymbol{M}_i\boldsymbol{O}_i}} \tag{22}$$

Since S_{in} and S_{ds} are the most important terms in the right hand side of Eqs. (1) in deep water, C_{ds} and δ_1 in *ST3* package, and a_1 and a_2 in *ST6* package should be determined. For *ST3* package, C_{ds} values from −5.5 to −1.5 with incremental step of 1, and five values 0, 0.3, 0.5, 0.7 and 1 for δ_1 parameter were considered. Moreover, original WAM-Cycle4 edition values (C_{ds}=−4.5 and δ_1=0.5) were utilized in calibration. For *ST6* package, several tuning values for a_1 were considered in the range of 3.74×10^{-8}–4.75×10^{-6}, while a_2 values were selected in the range of 1.24×10^{-6}–7×10^{-5}. Upper limits for a_1 and a_2 were default values in the WWIII model version 6.07. Suggested tuning values for *ST3* and *ST6* packages were used by Beyramzadeh et al. (2021) for model calibration in the Persian Gulf and Gulf of Oman.

Having the minimum error in the calibration process based on three buoys might result in tuning values which might not be appropriate for entire computational domain. The wave height along altimeter tracks provided opportunity to define a more robust optimization criterion. In addition to the total energy of spectrum, the frequency distribution of energy is also important for model assessment; hence, T_m is also considered in the calibration process according to Eq. (23). The pair of tuning values for both *ST3* (C_{ds} and δ_1) and *ST6* (a_1 and a_2) packages which resulted in the lowest ϵ would be considered as the optimum scenario.

$$\epsilon = \sum_{i=1}^{3}\left(\left|\boldsymbol{NMB}_{\boldsymbol{H_sBuoy}}\right| + \boldsymbol{HH}_{\boldsymbol{H_sBuoy}}\right)_i + \sum_{i=1}^{3}\left(\left|\boldsymbol{NMB}_{\boldsymbol{T_mBuoy}}\right| + \boldsymbol{HH}_{\boldsymbol{T_mBuoy}}\right)_i + \left(\left|\boldsymbol{NMB}_{\boldsymbol{Altimeter}}\right| + \boldsymbol{HH}_{\boldsymbol{Altimeter}}\right) \tag{23}$$

It is noteworthy to mention that the data corresponding to measured $H_s<$ 0.5 m were eliminated for skill assessment of WWIII model following (Beyramzadeh et al., 2021; Kazeminezhad and Siadatmousavi, 2017).

As shown in Fig. 8a, C_{ds}=−2.5 for *ST3* package led to the lowest *NMB, HH* and *SI* indices for H_s in Fig. 8a. Using lower values for δ_1 slightly enhanced the model performance in reproducing H_s. Moreover, as shown in Fig. 8b, δ_1=0.0 or 0.3 resulted in better performance in reproducing T_m. Regarding the ϵ error designated in Fig. 8c, C_{ds}=−2.5 and δ_1=0.3 provided the best performance (ϵ=1.0545); hence C_{ds}=−2.5 and δ_1=0.3 were considered as the optimum scenario when *ST3* package was employed in the WWIII model. The ϵ error with C_{ds}=−1.5 or −2.5 was almost insensitive to δ_1 variation, while higher values of δ_1 parameter with C_{ds}=−3.5 or −5.5 led to higher ϵ error.

For *ST6* package, a_1=3.74 $\times10^{-7}$ and a_2=5.24 $\times10^{-6}$ led to the lowest *NMB* for H_s, while a_1=5.5 $\times10^{-7}$ and a_2=1 $\times10^{-6}$ resulted in slightly lower *HH* and *SI* indices (see Fig. 8d). Unlike H_s, higher *NMB, HH* and *SI* indices for T_m were obtained by applying values higher than 3.74 $\times10^{-7}$ and 5.24 $\times10^{-6}$ for a_1 and a_2 parameters (see Fig. 8e). As shown in Fig. 8f, a_1=3.74 $\times10^{-7}$ and a_2=5.24 $\times10^{-6}$ resulted in the lowest ϵ = 1.1539 value; therefore, it was selected as the optimum tuning values for *ST6* package. It is also proposed by Zieger et al. (2015) as default values in WWIII model version 5.16.

Unlike *ST3*, the package *ST6* was less sensitive to the changes in tuning values. This pattern was reported before for the Persian Gulf (Beyramzadeh et al., 2021). Moreover, the total error value of ϵ was 1.0545 for *ST3* while it was equal to 1.1539 for *ST6*; therefore, the overall performance of WWIII model with *ST3* was better than with *ST6* for the considered period. The superiority of SWAN model with WAM-Cycle4 for the GOM, Puerto Rico and the U.S. Virgin Islands was reported recently by Allahdadi et al. (2021).

Swell dissipation terms in both *ST3* and *ST6* packages added two more unknown parameters s_1 and b_1 in the calibration procedure. Furthermore, a_0 for the effects of opposite wind is the other tuning value which should be determined. All presented results for *ST3* in Fig. 8a-c assumed s_1=0 which is the default value for WAM-Cycle4. The simulation with s_1=1 was repeated for the optimum tuning values introduced for *ST3* package (C_{ds}=−2.5 and δ_1=0.3). Obtained ϵ for s_1=1 was higher than for s_1=0. In addition, the results in Fig. 8d-f were provided assuming a_0=0.09 and b_1=0.0041 which were default values in WWIII model version 6.07. In this study three extra setup of values for a_0 and b_1 were evaluated: (1) a_0=0.04 and b_1=0.00025 used as the default values in WWIII model version 4.18; (2) a_0=0.09 and b_1=0.0032 proposed by WWIII model version 5.16; (3) a_0=0.11 and b_1=0.0038 suggested by Chen et al., 2019. None of these values for a_0 and b_1 could improve the model performance, and therefore a_0=0.09 and b_1=0.0041 were considered as the best option.

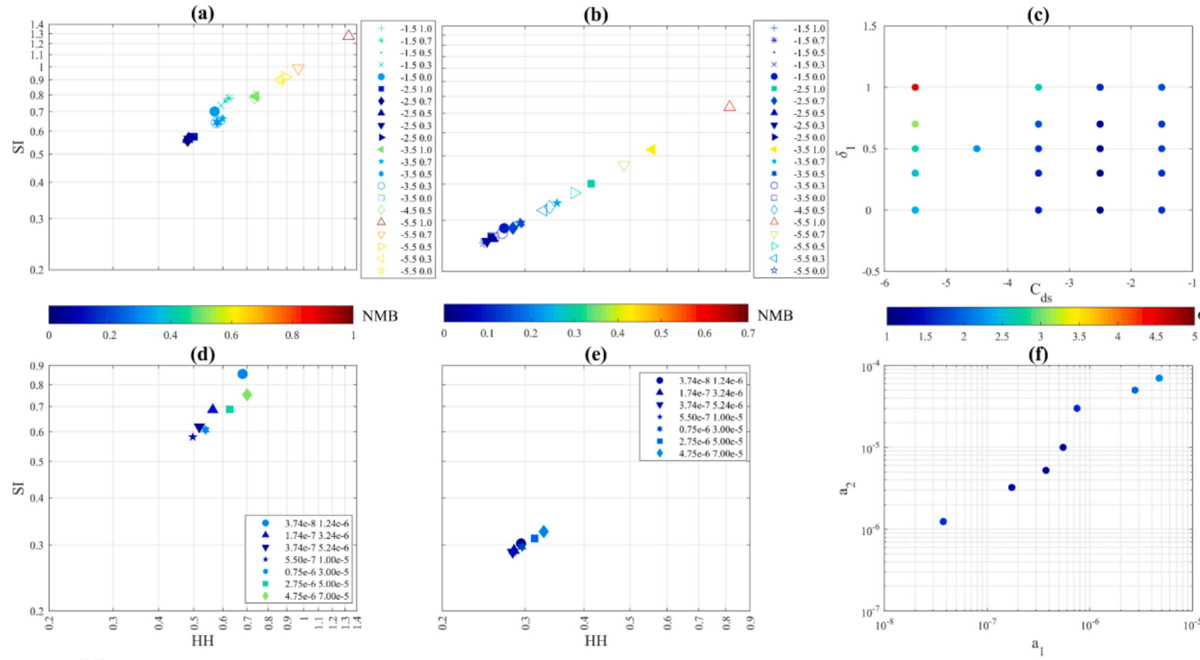

Fig. 8. Estimated *NMB, HH, SI*, and ϵ for *ST3* and *ST6* packages were showed in (a–c) and (d–f), respectively. First column relates to $\boldsymbol{H_s}$ and second one is for $\boldsymbol{T_m}$ parameter. In first and second columns, the summation of the absolute value of *NMB*, estimated in three deep water buoys ($\sum_{i=1}^{3}|\boldsymbol{NMB_i}|$) was presented with colors (blue color at lower-left side is optimum condition). Horizontal and vertical axes in first and second columns are in logarithmic scale. The values of ϵ error from Eq. (23) with respect to considered tuning values were presented in the third column.

5. Result

Results are presented using the optimum tuning values found in Section 4.2; i.e. C_{ds}=−2.5 and δ_1=0.3 for *ST3* and a_1=3.74 ×10^{-7} and a_2=5.24 ×10^{-6} for *ST6* package.

5.1. Comparison against NDBC buoys

Time series of H_s, T_m and wave direction were compared to *in-situ* measurements by *ST3* and *ST6* packages in Figs. 9 and 10 respectively. Although NDBC 42055 was adjacent to the path of the Hurricane Harvey (see Fig. 6), these extreme waves were not recorded by NDBC 42055. Unlike NDBC 42055, NDBC buoys 42019, 42035, 42001 and 42002 recorded H_s in the range of 3–8 m on 25–27 August. NDBC buoys 42001 and 42002 experienced high waves in the range of 3–4 m on 10–12 September. Similar pattern was observed for NDBC buoys 42012 and 42040 in Fig. 10. These two buoys experience H_s in the range of 3–4 m on 31 August and 10–12 September, while NDBC buoys 42036 and

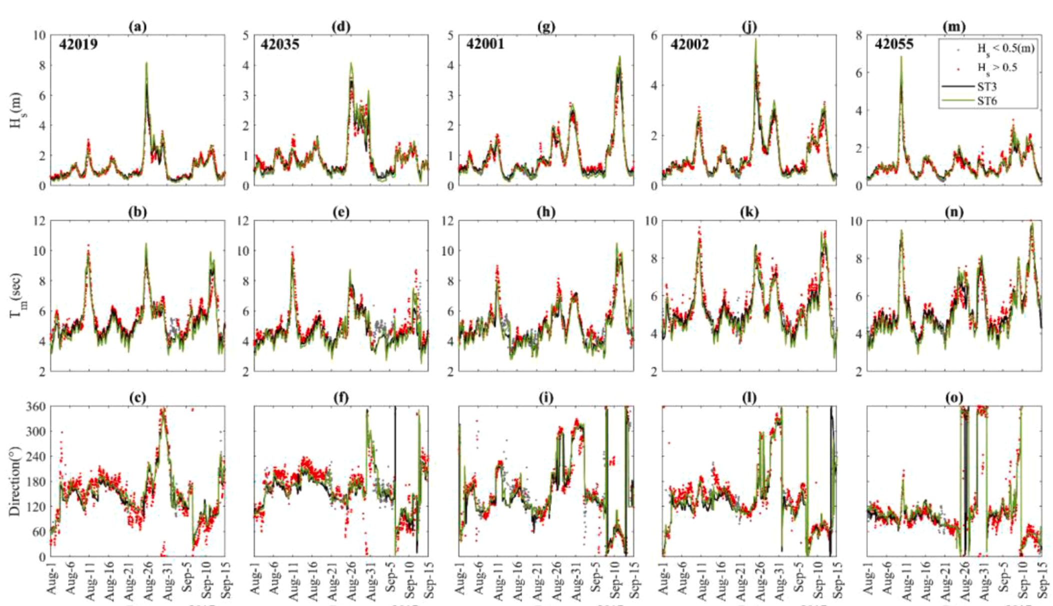

Fig. 9. Simulated $\boldsymbol{H_s}$, $\boldsymbol{T_m}$ and direction by *ST3* (black solid line) and *ST6* (green solid line) are compared with buoy measured data at NDBC 42019 (a–c), NDBC 42035 (d–f), NDBC 42001 (g–i), NDBC 42002 (j–l) and NDBC 42055 (m–o). Measured data with grey (red) dots are related to $\boldsymbol{H_s}$ values lower (higher) than 0.5 m, respectively. (For interpretation of the references to color in this figure legend, the reader is referred to the web version of this article.)

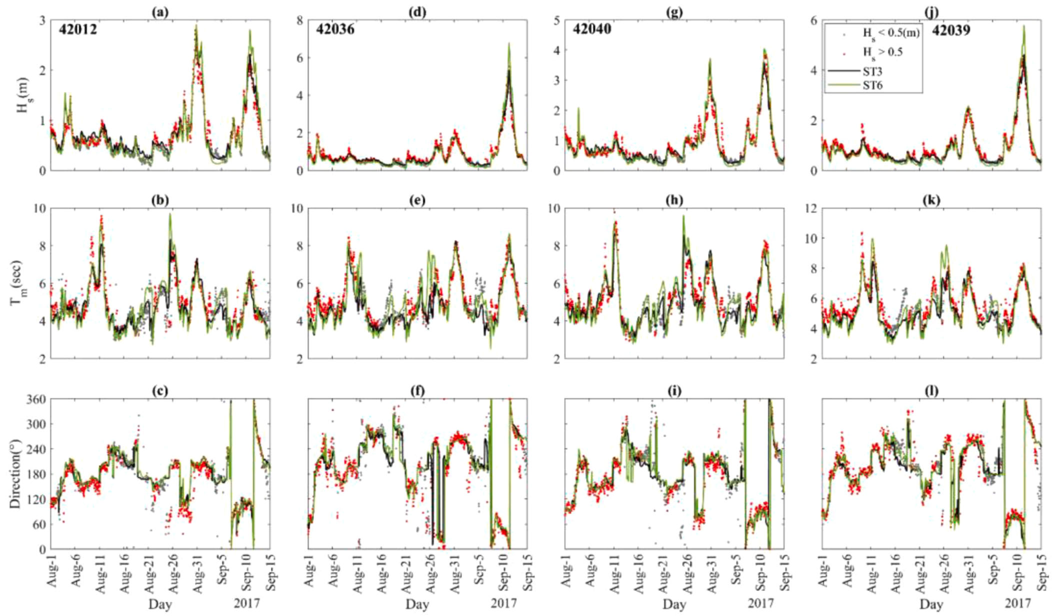

Fig. 10. Simulated H_s, T_m and direction by *ST3* (black solid line) and *ST6* (green solid line) are compared with buoy measured data at NDBC 42012 (a–c), NDBC 42036 (d–f), NDBC 42040 (g–i) and NDBC 42039 (j–l). Measured data with grey and red dots are related to H_s values lower and higher than 0.5 m, respectively. (For interpretation of the references to color in this figure legend, the reader is referred to the web version of this article.)

42039 experienced only one higher peak wave height in the range of 5–7 m on 10–12 September which was associated with passage of the Hurricane Irma over the GOM.

The *ST6* package slightly outperformed *ST3* package in the prediction of extreme wave height. This is in accordance with results of (Chen et al., 2019). In general, the performance of both *ST3* and *ST6* packages was similar in prediction of H_s; however, T_m was overestimated by *ST6* package. This deficit was more intense for buoys close to the Hurricane Irma track. Both packages were successful in reproducing the wave direction. Note that some inconsistencies between simulated T_m or wave direction and *in-situ* observations coincided with the time period in which H_s< 0.5 m.

5.2. Comparison against altimeter data

Altimeter-derived H_s is a great opportunity to evaluate the performance of WWIII model over the entire computational domain. Simulated H_s using both *ST3* and *ST6* packages were compared against altimeter wave height in Fig. 11. The almost zero mean bias occurred over the computational domain as shown in Fig. 11b and d; however,

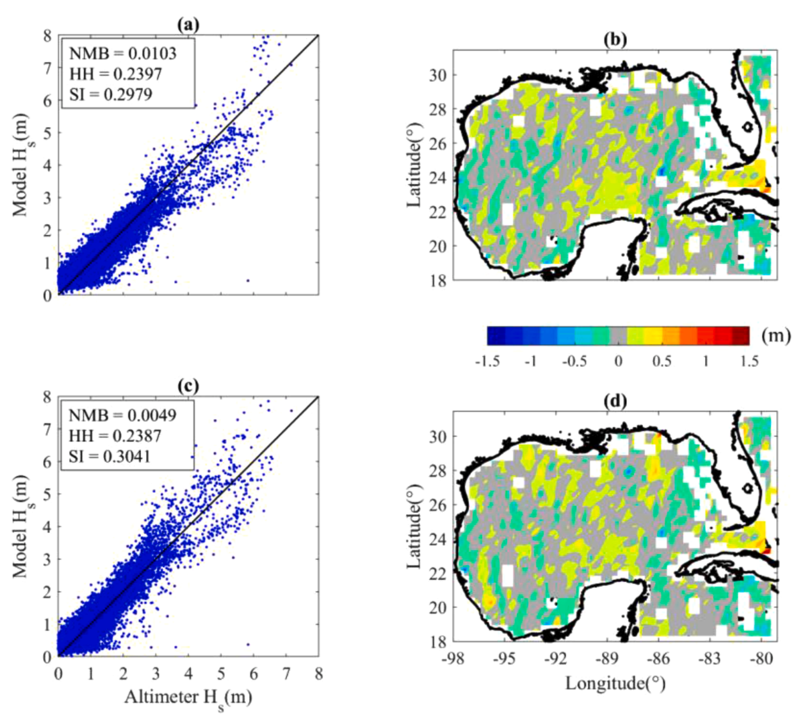

Fig. 11. The scatter plat of simulated wave height against altimeter recorded wave height with using *ST3* (a) and *ST6* (c). The distribution of mean bias over the computational domain obtained by *ST3* (b) and *ST6* (d).

slight underestimation of H_s using both *ST3* and *ST6* packages occurred in the western part of the GOM. This trend could be related to wind speed underestimation by ERA5 relative to altimeter recorded wind speed presented in Fig. 7b. In general, the model results were in good agreement with altimeter-derived H_s.

5.3. Using GMD and GQM for S_{nl} in a real wave field simulation

According to the results presented in Sections 4.2, 5.1 and 5.2, the performance of *ST3* and *ST6* was similar for H_s but *ST3* outperformed *ST6* for T_m estimation; therefore *ST3* was used in this section. The GMD method was considered in simulations with three-parameter quadruplet layout (λ, μ and θ) and ten representative quadruplets (Tolman, 2013). Since the formula presented in Section 2.4 is developed for deep water, the Eq. (12) was used to include the depth scale effects in GQM.

The optimum tuning values C_{ds}=−2.5 and δ_1=0.3 for whitecap dissipation term in *ST3* package are not necessarily led to the best performance when GMD or GQM was used for S_{nl} term; therefore, the calibration procedure described in section 4.2 was repeated when S_{nl} term was estimated by those methods. The optimum values of C_{ds}=−2.5 and δ_1=0.0 for *ST3* package was found when GMD was employed, while C_{ds}=−2.0 and δ_1=0.0 provided the best performance when GQM was used for S_{nl} term. The predicted H_s and T_m by obtained optimum tuning values for DIA, GMD and GQM methods were compared against buoy measured data in Fig. 12. Moreover, (C_{ds}=−2.0, δ_1=0.0) and (C_{ds}=−2.5, δ_1=0.0) with DIA, (C_{ds}=−2.0, δ_1=0.0) and (C_{ds}=−2.5, δ_1=0.3) with GMD, (C_{ds}=−2.5, δ_1=0.0) and (C_{ds}=−2.5, δ_1=0.3) in combination with GQM were added for more evaluations.

Estimated *NMB* index for H_s parameter using GMD with C_{ds}=−2.5, δ_1=0.0 and GQM with C_{ds}=−2.0, δ_1=0.0 were ~0.02-0.04 lower than DIA method with C_{ds}=−2.5, δ_1=0.3 setup in both shallow and intermediate water buoys. Note that DIA method with C_{ds}=−2.5, δ_1=0.3 outperformed GMD and GQM with their optimum setups regarding *HH* and *SI* indices (see Fig. 12a). The DIA method with C_{ds}=−2.5, δ_1=0.0 and C_{ds}=−2.5, δ_1=0.3 setups resulted in good statistical indices for T_m parameter at all three buoys groups in Fig. 12b.

To determine the best configuration, the combined error ϵ was evaluated as designated in Fig. 12c. The results of DIA with C_{ds}=-2.5, δ_1=0.0 and C_{ds}=−2.5, δ_1=0.3 were close but the lowest ϵ error occurred at all three buoys groups using δ_1=0.3. In the following section, DIA was used with C_{ds}=−2.5 and δ_1=0.3 for more model assessment in reproducing observed wave spectrum evolution.

5.3.1. Spectrum evolution

The spectrum evolution provides unique information about the distribution of wave energy over the frequencies and directions. The modeled and observed spectrum evolution at several NDBC buoys were compared in Fig. 13. The results indicated that the predicted wave spectrum evolutions using *ST3* in combination with the DIA method were in good agreement with buoy measurements during both fair and extreme weather conditions. The maximum error occurred mainly close to the peak frequency of the spectrum on 25–27 August and on 10–12 September which coincided with the dominance of Hurricanes Harvey and Irma in the GOM. Similar finding was previously reported for modeling the Hurricanes Gustav and Ike (2008) in the GOM (Siadatmousavi et al., 2012).

Simulated wave frequency spectra using *ST3* package in combination with DIA, GMD and GQM methods were evaluated for 25–27 August and 10–12 September periods using root mean square error (RMSE) and index of agreement (*d*) (Willmott, 1982) in Fig. 14. The index of agreement varies between 0 and 1 where 1 indicates the highest agreement between observation and model, while 0 denotes complete model failure. RMSE directly depends on wave energy content (i.e. H_s); therefore, higher RMSE was expected at NDBC buoys which experienced higher H_s during the dominance of Hurricanes Harvey and Irma (see NDBC buoys 42019, 42002 and 42036 in Figs. 10 and 14).

Although DIA, GMD and GQM methods mostly resulted in similar mean RMSE and index of agreement as shown in Table 2, the superiority of DIA in reproducing *in-situ* one-dimensional wave frequency spectra at most of NDBC buoys was obvious.

5.3.2. Sensitivity of directional wave spectra to nonlinear wave interaction term

One-dimensional wave spectra describe the distribution of wave energy over the frequencies. In contrast, the directional wave spectra depict the evolution of energy over both frequencies and directions.

Two snapshots were selected for NDBC buoys 42035, 42012 and 42040. In all selected snapshots, wind speed was greater than 10 m/s and $H_s \geq 1$ m. For NDBC 42035, the time of 0400 on 25 August was selected as a representative time before the Hurricane Harvey reached to this station. Also 0000 on 26 August was selected when peak wave height of 4 m occurred. NDBC buoys 42012 and 42040 experienced ~2 and ~4 m wave height, respectively at 0000 UTC on 11 September. Moreover, sudden wind and wave rotation from easterly to northerly was observed from 1500 to 1800 on 11 September; hence, 0200 on 12 September was selected for both buoys to evaluate the response of the

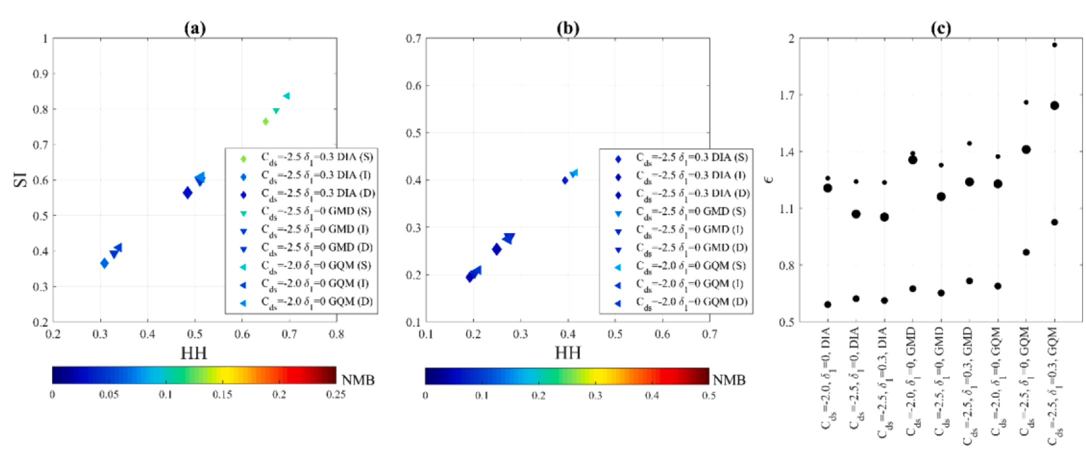

(a) (b) (c)

Fig. 12. The model performance with different scenarios are shown in terms of *HH* and *SI* for (a) $\boldsymbol{H_s}$ (a) and (b) $\boldsymbol{T_m}$. The summation of absolute values of *NMB* at shallow (small size markers 'S'), intermediate (medium size markers 'I') and deep water buoys (large size markers 'D'), were provided with different colors in these panels. The combined error ϵ was shown in panel (c). Three different marker size for each setup of the WWIII model in (c) are the same as (a) and (b). (For interpretation of the references to color in this figure legend, the reader is referred to the web version of this article.)

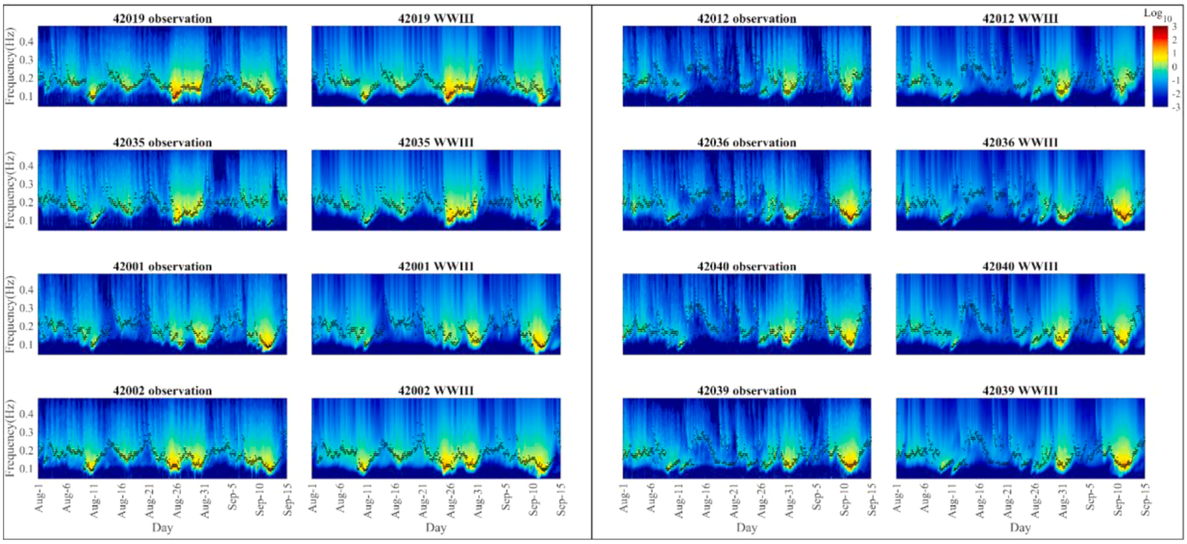

Fig. 13. The evaluation of simulated wave spectrum using *ST3* package with the DIA. Left (right) solid black box relates to buoys mainly affected by the Hurricane Harvey (Irma). In each boxes, left panels are related to observed and right panels are related to modeled spectrum evolution. The black dots in all panels show the peak frequency.

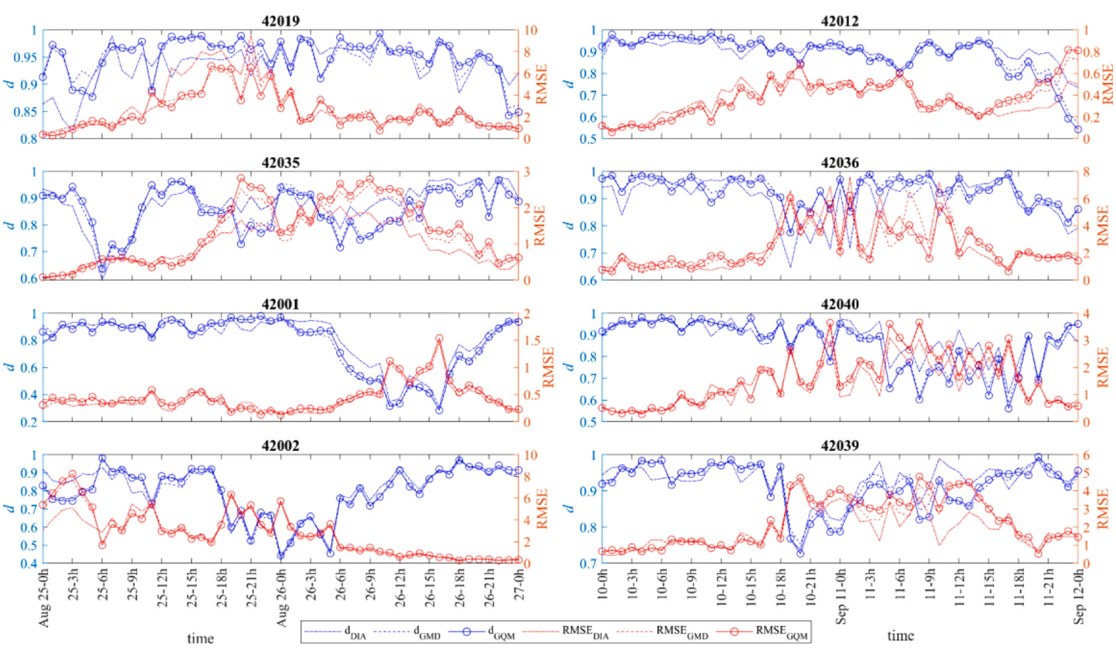

Fig. 14. Time series of RMSE and *d* indices for one-dimensional wave spectra. Left (right) panels present results at buoys mainly affected by the Hurricane Harvey (Irma).

Table 2
Mean RMSE and index of agreement (*d*) for periods of 25–27 August and 10–12 September at eight selected buoys. Bold italic values in each row relates to best method (highest *d* and lowest RMSE) at each buoy.

NDBC buoys	Mean Index of agreement (d) DIA	GMD	GQM	Mean RMSE DIA	GMD	GQM
42019	0.9355	0.9488	***0.9516***	2.9835	2.5718	***2.4957***
42035	***0.8746***	0.8639	0.8545	***0.9917***	1.1974	1.3342
42001	***0.8081***	0.7764	0.7852	***0.4220***	0.4591	0.4572
42002	***0.8016***	0.7856	0.7930	***2.5286***	2.8095	2.8165
42012	***0.9045***	0.8919	0.8887	***0.3455***	0.3694	0.3776
42036	0.8974	***0.9322***	0.9305	2.6115	***2.3567***	2.4216
42040	***0.8822***	0.8610	0.8572	***1.3888***	1.5461	1.5717
42039	***0.9243***	0.9193	0.9127	***1.8785***	2.1779	2.3084

wave model to wind veering.

Simulated directional wave spectra by DIA, GMD, GQM and WRT methods were compared with the measured one at NDBC buoys 42035, 42012 and 42040 in Fig. 15. The measured directional wave spectra were much wider than predicted one; most likely due to the low resolution of directional wave spectrum predicted by the Longuet-Higgins method from buoys motions (Young, 2006; Earle et al., 1999). The GQM and GMD methods were in good agreement with the WRT method. In contrast, directional wave spectra by the DIA method were broader than others. This problem in the DIA method had been shown for simple test cases in Section 2.5.1. Moreover, predicted peak energy by the DIA method was less energetic than others. The wind veering to the north was well simulated by all methods at NDBC buoys 42012 and 42040. In all snapshots, both measured and simulated peak frequencies were lower

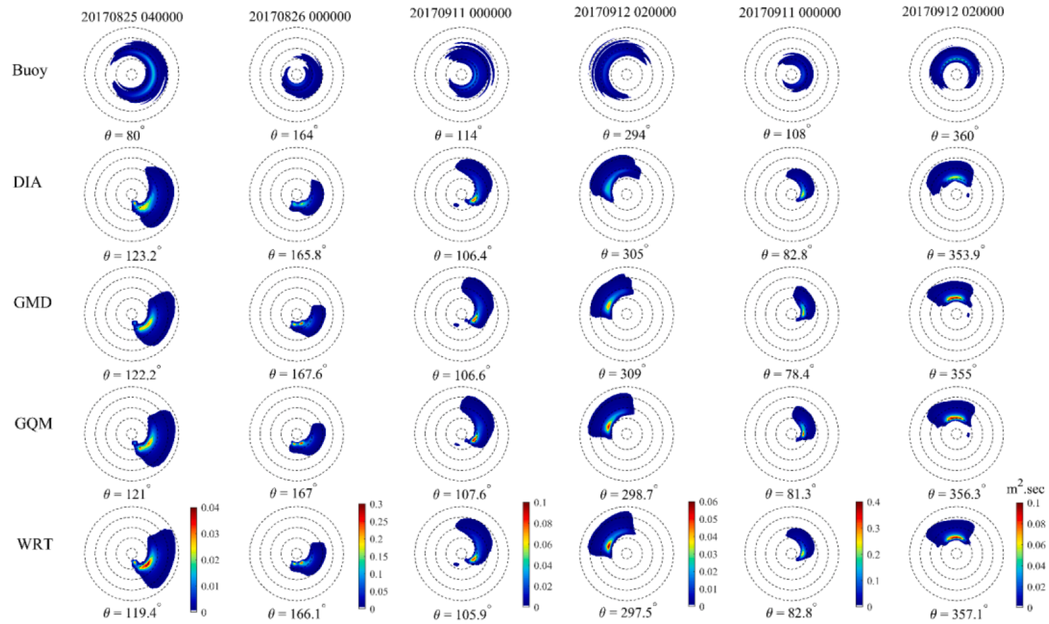

Fig. 15. The comparison between buoys and simulated directionoal wave spectra at NDBC 42035 (first and second columns), NDBC 42012 (third and fourth columns) and NDBC 42040 (fifth and sixth columns). Five dashed-circles from inner to outer one related to 0.05, 0.15, 0.25, 0.35 and 0.45 Hz. Colrobars are presented at the lowest end of each column. The θ values depict peak wave directions.

than 0.25 Hz.

6. Summary and conclusions

ERA5 wind data in combination with *ST3* and *ST6* packages were employed in the WWIII model to simulate the wave regime of the Gulf of Mexico (GOM) from August to 15 September in 2017. Observations from nine NDBC buoys including bulk wave parameters, meteorological and spectral data were considered for model assessment. This host of buoys network covers the GOM from deep water to continental shelf. Three deep water buoys 42001, 42002 and 42055 were used for the calibration of S_{ds} term in the model. Using only H_s parameter in the calibration procedure would result in weak performance for T_m prediction. Moreover, altimeter data from entire GOM can be used for model assessment as well; therefore, a combined error ϵ was introduced in present study. The calibration procedure suggested C_{ds}=−2.5 and δ_1=0.3 for *ST3* and a_1=3.74 $\times 10^{-7}$ and a_2=5.24 $\times 10^{-6}$ for *ST6* packages as the optimum tuning values. The obtained ϵ was lower for *ST3* package than for *ST6* package.

The time series of simulated H_s, T_m and wave direction using both *ST3* and *ST6* packages were compared with buoys measurements. Despite the fact that *ST6* slightly outperformed *ST3* in reproducing high waves during the dominance of Hurricanes Harvey and Irma, estimated T_m by *ST3* packages was more accurate than *ST6*. Wave direction was well estimated by both packages. The variations of wind in scales less than resolution of wind input to the model is important for low energy events. In fact, some inconsistencies also occurred between modeled and measured data when H_s<0.5 m and these data were eliminated from model assessments. The spatial distribution of mean bias and estimated statistical indices proved that model results were in well agreement with altimeter data.

The GQM was implemented in the WWIII model and used along with available methods DIA, GMD, and WRT methods for simple duration- and fetch-limited test cases. The results from GMD and GQM were similar to WRT, while DIA results were not in accordance with WRT results. Slanting fetch-limited test proved the reliability of GQM, while inconsistent results were obtained by the DIA and the GMD methods. The accuracy of GQM increased with increasing the accuracy of integration resolution. On the other hand, increasing the resolution needs more computational resources. The medium resolution was shown to be sufficiently accurate and feasible to be used in an operational wave model. Although the GQM method with medium resolution was ~200 times more time-consuming than DIA, it could be ~10 times faster than WRT method.

The white capping term of *ST3* was calibrated for each nonlinear interaction term in the WWIII model and used to simulated wave spectrum within the Gulf of Mexico (GOM). Regarding the introduced error ϵ, the DIA with C_{ds}=−2.5, δ_1=0.3 was the best setup for all buoys at shallow, intermediate and deep waters. The WWIII model with DIA method could reasonably well reproduced the frequency spectrum for the time period from 1 August to 15 September 2017. The maximum discrepancies between model and *in-situ* data occurred at the vicinity of the peak frequency within 25–27 August and 10–12 September in which the Hurricanes Harvey and Irma were dominant in the GOM. The general characteristics of *in-situ* directional wave spectra were well captured by all DIA, GMD, GQM and WRT methods; however, the wave spectrum predicted by GMD and GQM were similar to the result of WRT method for this time period. The DIA method resulted in directionally broad wave spectra and low wave energy contents at peak frequencies. Unlike these deficiencies in the DIA term, it led to superior performance of the WW3 model than inclusion of more accurate nonlinear interaction terms. The development of other source terms in the third generation wave models; especially white capping term, in combination with DIA over the last few decades is most likely the main reason for such surprising behavior. Therefore, in order to have more accurate wave simulation results, a redesign and recalibration of S_{ds} and S_{in} terms are needed, in addition to use a more accurate S_{nl} term than DIA.

CRediT authorship contribution statement

Mostafa Beyramzadeh: Writing – original draft, Conceptualization, Methodology, Validation. **Seyed Mostafa Siadatmousavi:** Writing – review & editing, Conceptualization, Supervision.

Declaration of Competing Interest

The authors declare that they have no known competing financial interests or personal relationships that could have appeared to influence the work reported in this paper.

Data availability

All data sources have been mentioned in the text; they are public data and can be accessed from the original sources

Acknowledgment

The authors acknowledge the High Performance Computing (HPC) Center at Sharif University of Technology for providing computational resource that have contributed to this research.

References

Abdolali, A., van der Westhuysen, A., Ma, Z., Mehra, A., Roland, A., Moghimi, S., 2021. Evaluating the accuracy and uncertainty of atmospheric and wave model hindcasts during severe events using model ensembles. Ocean Dyn. 1–19.

Abolfazli, E., Liang, J.H., Fan, Y., Chen, Q.J., Walker, N.D., Liu, J., 2020. Surface gravity waves and their role in oceanatmosphere coupling in the Gulf of Mexico. J. Geophys. Res. Oceans 125, e2018JC014820.

Alipour, A., Siadatmousavi, S.M., Jose, F., 2021. Numerical simulation of waves in the Caspian Sea: calibration and verification of the observation-based source terms. Ocean Dyn. 71, 699–714.

Allahdadi, M.N., He, R., Ahn, S., Chartrand, C., Neary, V.S., 2021. Development and calibration of a high-resolution model for the Gulf of Mexico, Puerto Rico, and the US Virgin Islands: Implication for wave energy resource characterization. Ocean Eng. 235, 109304.

Amante C., Eakins B.W. ETOPO1 arc-minute global relief model: procedures, data sources and analysis. 2009.

Ardag, D., Resio, D.T., 2019. Inconsistent spectral evolution in operational wave models due to inaccurate specification of nonlinear interactions. J. Phys. Oceanogr. 49, 705–722.

Battjes, J., Janssen, J., 1978. Energy loss and set-up due to breaking of random waves. Coast. Eng. Proc. 1.

Benoit, M., 2005. Evaluation of methods to compute the non-linear quadruplet interactions for deep-water wave spectra. In: Proc 5th Int Symp on Ocean Wave Measurement and Analysis (WAVES'2005), pp. 3–7.

Benoit, M., 2007. Implementation and test of improved methods for evaluation of nonlinear quadruplet interactions in a third generation wave model. Coastal Engineering 2006: (In 5 Volumes). World Scientific, pp. 526–538.

Beyramzadeh, M., Siadatmousavi, S.M., Derkani, M.H., 2021. Calibration and skill assessment of two input and dissipation parameterizations in WAVEWATCH-III model forced with ERA5 winds with application to Persian Gulf and Gulf of Oman. Ocean Eng. 219, 108445.

Cavaleri, L., Rizzoli, P.M., 1981. Wind wave prediction in shallow water: Theory and applications. J. Geophys. Res. 86, 10961–10973.

Chang, T.-Y., Chen, H., Hsiao, S.-C., Wu, H.-L., Chen, W.-B., 2021. Numerical Analysis of the Effect of Binary Typhoons on Ocean Surface Waves in Waters Surrounding Taiwan. Front. Mar. Sci. 8, 749185.

Chen, W.-B., Lin, L.-Y., Jang, J.-H., Chang, C.-H., 2017. Simulation of typhoon-induced storm tides and wind waves for the northeastern coast of Taiwan using a tide-surge-wave coupled model. Water 9, 549.

Chen, W.-B., Chen, H., Hsiao, S.-C., Chang, C.-H., Lin, L.-Y., 2019. Wind forcing effect on hindcasting of typhoon-driven extreme waves. Ocean Engineering 188, 106260.

Donelan, M.A., Babanin, A.V., Young, I.R., Banner, M.L., 2006. Wave-follower field measurements of the wind-input spectral function. Part II: parameterization of the wind input. J. Phys. Oceanogr. 36, 1672–1689.

Earle, M., Steele, K., Wang, D., 1999. Use of advanced directional wave spectra analysis methods. Ocean Eng. 26, 1421–1434.

Esquivel-Trava, B., Ocampo-Torres, F.J., Osuna, P., 2015. Spatial structure of directional wave spectra in hurricanes. Ocean Dyn. 65, 65–76.

Fan, Y., Rogers, W.E., 2016. Drag coefficient comparisons between observed and model simulated directional wave spectra under hurricane conditions. Ocean Model. 102, 1–13.

Gagnaire-Renou E. Amélioration de la modélisation spectrale des états de mer par un calcul quasi-exact des interactions non-linéaires vague-vague 2009.

Gagnaire-Renou, E., Benoit, M., Badulin, S.I., 2011. On weakly turbulent scaling of wind sea in simulations of fetch-limited growth. J. Fluid Mech. 669, 178–213.

Gagnaire-Renou, E., Benoit, M., Forget, P., 2010. Ocean wave spectrum properties as derived from quasi-exact computations of nonlinear wave-wave interactions. J. Geophys. Res.: Oceans 115.

Group WID, 2016. NOAA/NWS/NCEP/MMAB Technical Note 329, p. 326.

Hashimoto, N., Kawaguchi, K., 2001. Extension and modification of discrete interaction approximation (DIA) for computing nonlinear energy transfer of gravity wave spectra. Ocean Wave Measure. Anal. 530–539, 2002.

Hasselmann, S., Hasselmann, K., Allender, J., Barnett, T., 1985. Computations and parameterizations of the nonlinear energy transfer in a gravity-wave specturm. Part II: parameterizations of the nonlinear energy transfer for application in wave models. J. Phys. Oceanogr. 15, 1378–1391.

Hasselmann K., Barnett T., Bouws E., Carlson H., Cartwright D., Enke K., et al. Measurements of wind-wave growth and swell decay during the Joint North Sea Wave Project (JONSWAP). Deutches Hydrographisches Institut; 1973.

Hasselmann, K., 1962. On the non-linear energy transfer in a gravity-wave spectrum Part 1. General theory. J. Fluid Mech. 12, 481–500.

Herterich, K., Hasselmann, K.F., 1980. A similarity relation for the non-linear energy-transfer in a finite-depth gravity-wave spectrum. J. Fluid Mech. 97, 215–224.

Holland, G.J., Belanger, J.I., Fritz, A., 2010. A revised model for radial profiles of hurricane winds. Monthly Weather Rev. 138, 4393–4401.

Hsiao, S.-C., Chen, H., Wu, H.-L., Chen, W.-B., Chang, C.-H., Guo, W.-D., et al., 2020. Numerical simulation of large wave heights from super typhoon Nepartak (2016) in the eastern waters of Taiwan. J. Mar. Sci. Eng. 3, 217.

Janssen, P.A., 1991. Quasi-linear theory of wind-wave generation applied to wave forecasting. J. Phys. Oceanogr. 21, 1631–1642.

Kahma, K.K., Calkoen, C.J., 1992. Reconciling discrepancies in the observed growth of wind-generated waves. J. Phys. Oceanogr. 22, 1389–1405.

Kalourazi, M.Y., Siadatmousavi, S.M., Yeganeh-Bakhtiary, A., Jose, F., 2020. Simulating tropical storms in the Gulf of Mexico using analytical models. Oceanologia 62, 173–189.

Kazeminezhad, M.H., Siadatmousavi, S.M., 2017. Performance evaluation of WAVEWATCH III model in the Persian Gulf using different wind resources. Ocean Dyn. 67, 839–855.

Komen, G., Cavaleri, L., Donelan, M., Hasselmann, K., Hasselmann, S., Janssen, P., 1994. Dynamics and Modelling of Ocean Waves. Cambridge University Press, p. 502p.

Lavrenov, I.V., 2001. Effect of wind wave parameter fluctuation on the nonlinear spectrum evolution. J. Phys. Oceanogr. 31, 861–873.

Liu, Q., Babanin, A., Fan, Y., Zieger, S., Guan, C., Moon, I.-J., 2017. Numerical simulations of ocean surface waves under hurricane conditions: assessment of existing model performance. Ocean Model. 118, 73–93.

Liu, Q., Rogers, W.E., Babanin, A.V., Young, I.R., Romero, L., Zieger, S., et al., 2019. Observation-based source terms in the third-generation wave model WAVEWATCH III: updates and verification. J. Phys. Oceanogr. 49, 489–517.

Moon, I.-J., Ginis, I., Hara, T., 2004. Effect of surface waves on air–sea momentum exchange. Part II: behavior of drag coefficient under tropical cyclones. J. Atmos. Sci. 61, 2334–2348.

Perrie, W., Toulany, B., Resio, D.T., Roland, A., Auclair, J.-P., 2013. A two-scale approximation for wave–wave interactions in an operational wave model. Ocean Model. 70, 38–51.

Resio, D., Perrie, W., 1989. Implications of an f− 4 equilibrium range for wind-generated waves. J. Phys. Oceanogr. 19, 193–204.

Resio, D.T., Perrie, W., 2008. A two-scale approximation for efficient representation of nonlinear energy transfers in a wind wave spectrum. Part I: theoretical development. J. Phys. Oceanogr. 38, 2801–2816.

Ribal, A., Young, I.R., 2019. 33 years of globally calibrated wave height and wind speed data based on altimeter observations. Sci. Data 6, 1–15.

Rogers, W.E., Van Vledder, G.P., 2013. Frequency width in predictions of windsea spectra and the role of the nonlinear solver. Ocean Model. 70, 52–61.

Romero, L., Melville, W.K., 2010. Airborne observations of fetch-limited waves in the Gulf of Tehuantepec. J. Phys. Oceanogr. 40, 441–465.

Shih, H.-J., Chen, H., Liang, T.-Y., Fu, H.-S., Chang, C.-H., Chen, W.-B., et al., 2018. Generating potential risk maps for typhoon-induced waves along the coast of Taiwan. Ocean Engineering 163, 1–14.

Siadatmousavi, S.M., Jose, F., da Silva, G.M., 2016. Sensitivity of a third generation wave model to wind and boundary condition sources and model physics: a case study from the South Atlantic Ocean off Brazil coast. Comput. Geosci. 90, 57–65.

Siadatmousavi, S.M., Jose, F., Stone, G., 2012. On the importance of high frequency tail in third generation wave models. Coastal Eng. 60, 248–260.

Sun, Y., Perrie, W., Toulany, B., 2018. Simulation of WaveCurrent Interactions Under Hurricane Conditions Using an UnstructuredGrid Model: Impacts on Ocean Waves. J. Geophys. Res. Oceans 123, 3739–3760.

Sun, R., Villas Bôas, A.B., Subramanian, A.C., Cornuelle, B.D., Mazloff, M.R., Miller, A.J., et al., 2022. Focusing and defocusing of tropical cyclone generated waves by ocean current refraction. J. Geophys. Res. Oceans, e2021JC018112.

Tamizi, A., Young, I.R., 2020. The spatial distribution of ocean waves in tropical cyclones. J. Phys. Oceanogr. 50, 2123–2139.

Tamizi, A., Alves, J.-H., Young, I.R., 2021. The physics of ocean wave evolution within tropical cyclones. J. Phys. Oceanogr.

Tolman, H.L., Grumbine, R.W., 2013. Holistic genetic optimization of a generalized multiple discrete interaction approximation for wind waves. Ocean Model. 70, 25–37.

Tolman, H., 2003. Tech. Note 227, NOAA/NWS/NCEP/MMAB, p. 57 pp.+ Appendices.

Tolman, H.L., 2013. A generalized multiple discrete interaction approximation for resonant four-wave interactions in wind wave models. Ocean Modell. 70, 11–24.

Webb, D., 1978. Non-linear transfers between sea waves. Deep Sea Res. 25, 279–298.

Willmott, C.J., 1982. Some comments on the evaluation of model performance. Bull. Am. Meteorol. Soc. 63, 1309–1313.

Xie, L., Bao, S., Pietrafesa, L.J., Foley, K., Fuentes, M., 2006. A real-time hurricane surface wind forecasting model: Formulation and verification. Monthly Weather Rev. 134, 1355–1370.

Young, I.R., Van Vledder, GP., 1993. A review of the central role of nonlinear interactions in wind—wave evolution. Philos. Trans. R. Soc. London Ser. A 342, 505–524.
Young, I.R., 2006. Directional spectra of hurricane wind waves. J. Geophys. Res. 111.
Young, I., Hasselmann, S., Hasselmann, K., 1987. Computations of the response of a wave spectrum to a sudden change in wind direction. J. Phys. Oceanogr. 17, 1317–1338.
Zieger, S., Babanin, A.V., Rogers, W.E., Young, I.R., 2015. Observation-based source terms in the third-generation wave model WAVEWATCH. Ocean Model. 96, 2–25.
Zijlema, M., Van Vledder, G.P., Holthuijsen, L., 2012. Bottom friction and wind drag for wave models. Coastal Eng. 65, 19–26.

Further Reading

Puscasu, R.M., 2014. Integration of artificial neural networks into operational ocean wave prediction models for fast and accurate emulation of exact nonlinear interactions. Procedia Comput. Sci. 29, 1156–1170.